

Mo Atom Rearrangement Drives Layer-Dependent Reactivity in Two-Dimensional MoS₂

Zifan Wang¹, Jiaxuan Wen², Tina Mihm³, Shaopeng Feng², Kelvin Huang³, Jing Tang⁴,

Tianshu Li⁴, Liangbo Liang⁶, Sahar Sharifzadeh³, Keji Lai², Xi Ling^{1, 4, 5*}

¹ Department of Chemistry, Boston University, Boston, Massachusetts 02215, USA.

² Department of Physics, The University of Texas at Austin, Austin, Texas 78712, USA.

³ Department of Electrical and Computer Engineering, Boston University, Boston, Massachusetts 02215, USA.

⁴ Division of Materials Science and Engineering, Boston University, Boston, Massachusetts 02215, USA.

⁵ The Photonics Center, Boston University, Boston, Massachusetts 02215, USA.

⁶ Center for Nanophase Materials Sciences, Oak Ridge National Laboratory, Oak Ridge, Tennessee 37831, USA.

*To whom the correspondence should be addressed. Email address: xiling@bu.edu

Abstract

Two-dimensional (2D) materials offer a valuable platform for manipulating and studying chemical reactions at atomic level, owing to the ease of controlling their microscopic structure at the nanometer scale. While extensive research has been conducted on the structure-dependent chemical activity of 2D materials, the influence of structural transformation during the reaction remains largely unexplored. In this work, we report the layer-dependent chemical reactivity of MoS₂ during a nitridation atomic substitution reaction and attribute it to the rearrangement of Mo atoms. Our results show that the chemical reactivity of MoS₂ decreases as the number of layers is reduced in the few-layer regime. In particular, monolayer MoS₂ exhibits significantly lower reactivity compared to its few-layer and multilayer counterparts. Atomic-resolution transmission electron microscope (TEM) reveals that MoN nanonetworks form as reaction products from monolayer and bilayer MoS₂, with the continuity of the MoN crystals increasing with layer number, consistent with the local conductivity mapping data. The layer-dependent reactivity is attributed to the relative stability of the hypothetically formed MoN phase which retain the number of Mo atomic layers present in the precursor. Specifically, the low chemical reactivity of monolayer MoS₂ is attributed to the high energy cost associated with Mo atom diffusion and migration necessary to form multi-layer Mo lattices in the thermodynamically stable MoN phase. This study underscores the critical role of lattice rearrangement in governing chemical reactivity and highlights the potential of 2D materials as versatile platforms for advancing the understanding of materials chemistry at atomic scale.

Key words: 2D materials, layer-dependent, chemical reactivity, Raman spectroscopy, Transmission electron microscope, DFT calculation

Introduction

Tailoring material structures to manipulate chemical reactions with atomic precision has become a central theme in modern material science.^{1–8} Two-dimensional (2D) materials provide a unique platform for studying chemistry at atomic level, due to the ease of control of their microscopic structures such as stacking configuration and thickness. In recent years, growing interest has emerged in exploring the correlation between the microscopic structure and chemical performance of 2D materials such as graphene and MoS₂.^{9–18} For instance, 1T phase transition metal dichalcogenides (TMDs) exhibit significantly higher reactivity in organohalides surface functionalization reaction, compared to the 2H phase.^{19,20} Layer-dependent chemical reactivity of MoS₂ was further reported in both ion-intercalation phase transition²¹ and the hydrogen evolution reaction (HER)²², which was attributed to the distinct electronic structure of MoS₂ with different numbers of layers. Similarly, strong thickness- and stacking-order-dependent surface functionalization has been observed in graphene.^{23,24}

In conventional models of chemical reactivity, the electronic properties of reactants are considered central to determining reaction rates, and this perspective is well captured by Marcus theory.^{25–28} Marcus theory has been widely applied to understand the electron-transfer reactions on 2D materials such as carbon nanotubes^{29–32} and graphene.^{12,24,33,34} However, the theory is based on the premise that the chemical species do not undergo significant lattice rearrangement during electron transfer, limiting its applicability in many reaction systems—particularly in solid-state transformations where the product lattice differs substantially from that of the precursor. For example, in a previously reported atomic substitution reaction converting van der Waals (vdW) layered MoS₂ into non-vdW molybdenum nitride (MoN),^{35–37} the process involves not only charge transfer between MoS₂ and NH₃, but also substantial crystal structure transformation from MoS₂ to MoN—extending beyond the scope of Marcus theory. Investigating how the reaction kinetics depend on the microscopic structure of MoS₂, such as the number of layers, could offer significant insights into the fundamental principles governing material reactivity.

Here, we use the atomic substitution reaction in MoS₂ as a model system to demonstrate that its layer-dependent chemical reactivity is driven by the Mo atom

rearrangement. We observe that thinner MoS₂ (e.g., monolayers and bilayers) exhibit significantly lower chemical reactivity compared to thicker counterparts. Using transmission electron microscope (TEM), we characterize the resulting MoN morphology and find that, while crystalline MoN forms across all precursor thicknesses, the microstructural morphology varies significantly. Specifically, MoN nanonetworks form from the reaction products of monolayer and bilayer MoS₂, whereas a continuous MoN film is observed when starting from thicker MoS₂. The results are consistent with local conductivity imaging by microwave impedance microscopy (MIM). To elucidate the layer-dependent chemical reactivity and the morphological evolution of the resulting MoN, we propose a mechanistic interpretation centered on the rearrangement of Mo atoms necessary for the formation of thermodynamically stable MoN structures. Density Functional theory (DFT) calculations investigate the initial step of the reaction and the binding mechanism of NH₃ to the MoS₂ surface.

Results and Discussion

We first demonstrate the layer-dependent reactivity on a step-shaped MoS₂ flake consisting of monolayer (1L), few-layer (FL) and multilayer (ML) regions. The sample is mechanically exfoliated and transferred onto a SiO₂/Si substrate, followed by a nitridation reaction with ammonia gas in a quartz tube furnace. Figure 1a and S1 in the Supplementary Information (SI) show the optical images of the sample at various stages of the reaction. As the reaction proceeds, pronounced changes in optical contrast are observed in the FL and ML regions, indicating the formation of MoN,^{35–37} also supported by the X-ray photoelectron spectroscopy (XPS) measurements (Figure S2). In contrast, the monolayer region shows no visible change in optical contrast, suggesting significantly lower reactivity. Notably, the thicker regions exhibit fast and more complete conversion. In the ML region, the reaction initiates within the first 3 mins and is completed by 15 mins. The FL region shows a delayed response, with surface conversion beginning at around 12 mins and completing at 27 mins. Remarkably, the 1L region remains unconverted even after 27 mins, with no observable contrast variation, highlighting its high chemical inertness under the same reaction conditions.

The thickness-dependent reactivity is further characterized by Raman spectroscopy, as shown in Figure 1b to 1d. After 15 mins of reaction, the E_{2g}^1 and A_{1g} modes of MoS₂ disappear in the ML region, while a new Raman peak at 211 cm⁻¹—attributed to the Mo₅N₆ phase^{35,38}—emerges, indicating the successful conversion of MoS₂. In the FL region, the two Raman modes of MoS₂ remain detectable even after 24 mins; however, their intensities significantly decrease, suggesting that a substantial portion of MoS₂ has been converted. In addition to the intensity decrease, a red shift of the E_{2g}^1 mode is observed, which is attributed to increased strain associated with the formation of shorter Mo-N bonds.^{39–41} The conversion in the FL region completes at around 27 mins, as evidenced by the disappearance of MoS₂ Raman signals and the appearance of a Mo₅N₆ Raman peak at 204 cm⁻¹.³⁸ In contrast, strong and well-defined Raman signals from MoS₂ persist in the 1L region after 27 mins of reaction. The slight reduction of intensity and peak broadening are attributed to the degradation of crystallinity and the slow thermal decomposition of monolayer MoS₂ under prolonged high temperature annealing.

We further performed TEM characterizations on a partially converted step-shaped MoS₂ flake. As shown in Figure 1e, the sample contains three distinct regions with thicknesses of 26.7, 6.3 and 3.3 nm, as measured by atomic force microscopy (AFM) prior to transfer onto a TEM grid. In the 26.7 nm and 6.3 nm regions, MoN-MoS₂ heterojunctions are clearly observed, with well-defined interfaces outlined by yellow dashed lines. This is corroborated by the presence of two distinct sets of selected area electron diffraction (SAED) patterns at the junctions. In contrast, no evidence of MoN formation is observed in the thinnest 3.3 nm region, displaying only a single set of SAED patterns corresponding to MoS₂. This results further confirm that thinner MoS₂ exhibits lower chemical reactivity in the nitridation reaction compared to thicker MoS₂.

We further probe the layer-dependent reactivity in the ultrathin regime through a comparative analysis of monolayer (1L), bilayer (2L), trilayer (3L) and quadrilayer (4L) domains. Figure 2a and Figure S4 show optical images of the ultrathin step-shaped MoS₂ sample, with each layer-thickness region labeled and separated by white dashed lines. The layer number of each region is determined through Raman and photoluminescence (PL) spectroscopy,^{42–44} as shown in Figure S3. Optical microscope, Raman intensity mapping

of the A_{1g} mode of MoS_2 , along with gigahertz conductivity mapping using microwave impedance microscopy (MIM)^{45,46} are used to monitor the reaction progress during nitridation. As the reaction proceeds, optical contrast changes—similar to those described in Figure 1a—are observed, further indicating layer-dependent reactivity even within the few-layer regime. In particular, the 3L and 4L regions show the onset of conversion at 6 mins, with significant transformation by 12 mins. In contrast, the 2L and 1L regions convert more slowly, with noticeable contrast changes at 14 and 18 mins, respectively. Although the reactivity difference between 3L and 4L is minimal, pronounced differences are observed among 1L, 2L and 3L regions. Especially, monolayer MoS_2 remains highly inert in the conversion, requiring 42 mins for complete conversion, consistent with our earlier findings.

These conclusions can be further supported by the Raman intensity mapping shown in Figure 2b. At 0 min, the Raman intensity increases progressively from the 1L to 4L region, primarily due to the optical interference effect associated with both laser excitation and Raman scattering.^{47–49} As the conversion proceeds, a substantial decrease in Raman intensity is observed across all four regions, reflecting the transformation of MoS_2 . However, the evolution of Raman intensities follows distinct trends in different layers. To elucidate these differences, we extract the average A_{1g} peak intensity from each region and perform a statistical analysis (see Methods), as presented in Figure 2d. At 6 min, the A_{1g} peak intensity decreases in all four regions—not primarily due to chemical conversion, but rather due to crystallinity degradation and the onset of slow thermal decomposition of MoS_2 , as previously mentioned. The magnitude of intensity reduction exhibits an inverse correlation with layer thickness—1L (25.2%), 2L (21.0%), 3L (18.3%), and 4L (10.9%)—suggesting that thinner MoS_2 exhibits lower thermal stability, consistent with prior reports.¹⁸ After an additional 6 min of annealing, a significant Raman intensity drop is observed in the 3L (55.0%) and 4L (49.5%) regions, indicating their conversion to MoN , while the 1L and 2L regions show invisible change, reflecting their lower reactivity. This observation is in excellent agreement with the optical contrast evolution. By 13 min, the A_{1g} peak intensities of both 4L and 3L drop to zero, indicating the full conversion on these two regions. The 2L region shows a significant intensity drop from 81.6% to 49.8% at 14 min, consistent with the partial conversion suggested by the optical images, and reaches

full conversion at 18 min, with the intensity decreases to zero. Notably, a residual A_{1g} peak intensity of 18.8% remains in the 1L region at 18 min, indicating incomplete conversion. The Raman intensity of 1L vanishes at 42 min—much later than that for 2L, highlighting remarkably lower reactivity of monolayer MoS_2 . These results further underscore the pronounced layer-dependent reactivity of MoS_2 and the exceptional chemical inertness of monolayer MoS_2 during the nitridation reaction.

Given the stark contrast in electrical properties between semiconducting MoS_2 and highly conductive MoN, conductivity maps obtained from MIM measurements (see Methods and Figure S6), provide a powerful tool to monitor the formation and nanoscale spatial evolution of MoN throughout the conversion reaction. As shown in Figure 2c, the pristine MoS_2 flake exhibits uniformly low conductivity across all regions, from 1L to 4L, prior to conversion, consistent with the intrinsic semiconducting nature of MoS_2 .^{43,50} At 6 min, a pronounced increase of conductance emerges, indicating the formation of metallic MoN in the corresponding regions.^{35,36} The signal is most prominent in the 4L region and along the boundary between the 4L and the 3L domains, suggesting a higher reactivity of these thicker regions compared to the 2L and 1L counterparts. As the reaction progresses, the high-conductance areas in the 4L and 3L regions expand and reach saturation at 13 min, marking their complete conversion to MoN, in agreement with the Raman results. A noticeable conductance increase is observed in the 2L region at 14 min with the contrast continuing to intensify until 18 min, corresponding to the partial and then full conversion of bilayer MoS_2 . Interestingly, no obvious MIM signal change is detected in the 1L region throughout the conversion, including at 42 min when Raman measurements confirm its full conversion. Additionally, MoN domains derived from thicker MoS_2 layers exhibit substantially higher electrical conductance than those converted from thinner layers. This observation implies a layer-dependent variation in the structural quality and morphology of the resulting MoN, highlighting the need for structural and morphological characterizations at nanometer scale to uncover the underlying mechanisms.

To understand the conductivity evolution and elucidate the mechanism underlying the layer-dependent reactivity, we perform TEM characterizations on a fully converted step-shaped MoS_2 flake containing regions from 1L to 4L (Figure S7). SAED patterns

acquired at various thicknesses uniformly exhibit a single set of hexagonal diffraction spots corresponding to the (100) planes of δ -MoN (Figure 3a and Figure S8), all aligned in the same crystallographic orientation. It should be noted that the emerging of δ -MoN phase is the result of higher conversion temperature (i.e. 680 °C) used to fully convert the MoS₂ samples at a higher reaction rate, in contrast to the samples in Figure 1 and 2 where a lower temperature was used for a better control of the reaction rate. This result implies the formation of highly orientated MoN domains with uniform lattice structure and crystallographic alignment across all precursor thicknesses, consistent with the epitaxial atomic substitution mechanism we proposed in previous work.³⁷ However, high-resolution transmission electron microscopy (HRTEM) images reveal substantial differences in the morphology of the MoN products derived from different initial layer numbers of MoS₂ (Figure 3b, Figure S10 to S15). The MoN domains can be readily distinguished from the underlying amorphous SiN membrane due to their higher contrast. In the 1L and 2L regions, the δ -MoN forms discontinuous networks composed of nanoscale crystallites interspersed with voids, resulting in a nanonetwork morphology. In the 3L region, the void density decreases significantly, and the δ -MoN adopts a more continuous and uniform structure. This trend continues in the 4L region, where a nearly void-free, continuous δ -MoN film is observed. This evolution from discontinuous to continuous morphology with increasing precursors thickness provides a structural basis to understand the layer-dependent MIM signals discussed above. The 1L region is highly fragmented with small grains disconnected from each other, leading to very weak signals in MIM, which measures the overall sheet conductance at the 50 ~ 100 nm length scale. While the film is still fractured in the 2L region, the underlying connectivity is much improved, resulting in significantly stronger MIM signals. Starting from 3L and above, the δ -MoN crystals become more continuous and better connected, which explains the much higher sheet conductance in the MIM data.

Importantly, these morphology differences also provide insights into the mechanistic origin of the layer-dependent reactivity. Previous studies have established that the thermodynamically stable δ -MoN phase possesses a unit cell comprising two hexagonal close-packed Mo atomic layers, with nitrogen atoms arranged in an ABAB stacking sequence at the interstitial sites.^{51–57} The formation of this structure from a monolayer

MoS₂ precursor requires significant atomic rearrangement, including the vertical migration of Mo atoms to form a multilayered configuration along the c-axis. As a result of the atomic rearrangement, MoN crystals converted from monolayer MoS₂ precursor are discontinuous, and thus less electrically conductive. Moreover, since a single-unit-cell MoN structure is less stable than those containing multiple Mo atomic layers, the 2L and 3L regions are expected to undergo a certain degree of vertical Mo atom migration to form a more thermodynamically favorable MoN configuration, resulting in voids in the products. Notably, this rearrangement introduces an energetic barrier that renders the transformation less kinetically favorable, particularly in ultrathin regions with limited Mo atoms available in the out-of-plane direction. As a result, thinner MoS₂ films, especially monolayers, exhibit reduced reactivity and slower conversion kinetics—consistent with the delayed transformation. Structural reordering of MoS₂ layers involving Mo migration and agglomeration has been previously observed under external energy input, such as joule heating⁵⁸ and low-energy ion irradiation⁵⁹, offering further rational for our proposed mechanism. Figure 3c provides a schematic illustration of the conversion process in 1L and 4L MoS₂, highlighting the morphology difference that arises from their distinct structural transformation pathways. In 4L MoS₂, nearly no vertical rearrangement of Mo atoms is required to form an energetically favorable MoN structure, thereby preserving the structural continuity of the product. In contrast, in 1L MoS₂, substantial vertical rearrangement of Mo atoms is necessary to attain a thermodynamically stable MoN phase, leading to the formation of intergranular voids between MoN nanocrystals. In MoS₂ layers of specific thickness, the structural transformation pathway is governed by a trade-off between the thermodynamic stability of the resulting MoN phase and the energetic cost associated with vertical rearrangement of Mo atoms.

To further support our mechanistic interpretation, we quantitatively analyze the lateral coverage of the resulting MoN films based on TEM images (Figure 3d). The conversion process induces a reduction in lateral film coverage due to both vertical Mo atom rearrangement and lattice mismatch between MoS₂ and MoN. In the absence of vertical Mo atom rearrangement, the lattice constant difference between MoS₂ (i.e. 3.19 Å) and MoN (i.e. 2.89 Å) leads to a projected coverage of $2.89^2 / 3.19^2 = 82.1\%$, corresponding to an ‘N-to-N’ conversion scenario in which the number of Mo atomic layers is preserved.

If half of the Mo atoms migrate out-of-plane to form an additional Mo layer, the expected lateral coverage decreases to $0.5 \times 2.892 / 3.192 = 41.0\%$, corresponding to an ‘N-to-2N’ conversion.

The measured MoN coverages for regions converted from 1L and 2L MoS₂ are 44.48% and 46.94%, respectively, which are in close agreement with the ‘N-to-2N’ model. This suggests that monolayer MoS₂ is predominantly converted into a MoN structure containing two Mo atom layers, while bilayer MoS₂ is converted into a MoN structure containing four Mo atom layers. For the 3L region, the measured MoN coverage is 72.25%, which lies between the values predicted in the ‘N-to-N’ (82.1%) and ‘3L-to-4L’ (~62%) models. We believe in this case, approximately half of the Mo atoms in 3L MoS₂ undergo vertical rearrangement to form a four-Mo-layer MoN, while the other half retain their original plane following the ‘N-to-N’ model. Our previous work has shown that the MoN structure contains four Mo atom layers exhibits a higher thermodynamic stability compared to three-layer variants,³⁸ which further support this “3L-to-4L” transformation preference in the 3L case. We also noticed that the measured MoN coverage for 4L region is higher than the predicted values from both the “N-to-N” and “N-to-2N” models. This discrepancy is likely due to residual strain in the MoN film that is not fully released during the conversion process. The model predictions assume complete relaxation of the strain arising from the bond length mismatch between Mo–S and Mo–N. In practice, however, the presence of a supporting substrate makes full strain release difficult to achieve. Moreover, compared with the more interspersed MoN domains formed from thinner MoS₂ layers, the more uniform and continuous MoN film derived from 4L MoS₂ presents greater challenges for strain relaxation.

In addition to the energy barrier associated with Mo atom rearrangement for the formation of stable MoN phases, another factor that may contribute to the observed layer-dependent chemical reactivity is the adsorption behavior of NH₃ on MoS₂. To investigate this, we perform density functional theory (DFT) calculations to determine the dependence of NH₃ binding on MoS₂ layer number. Specifically, we computed the binding energies of a single NH₃ molecule on MoS₂ layers ranging from 1L to 4L. Given that MoS₂ used in our experiments is likely to contain native defects—particularly sulfur vacancies, which are

predicted to be the most stable intrinsic defects in MoS₂⁶⁰ we investigate NH₃ adsorption on both pristine and defective surfaces. Four types of defects are considered: 1) a single sulfur vacancy (V_S); 2) a defect cluster with three sulfur vacancies (V_{S3}); 3) a defect complex consisting of a single Mo vacancy with three neighboring sulfur atoms removed (V_{MoS3}); and 4) a larger defect complex involving the removal of three sulfur atoms and one Mo atom from a hexagonal ring (V_{MoS3, H}). Structural models of these defects are provided in Figure S16 of the SI. Although the latter two defect complexes are less energetically favorable (see Table S1 in the SI for calculated defect formation energies), they are included to represent potential reactive sites that may exist at step edges or grain boundaries in the experimental samples, or that may form during high-temperature annealing.

Figure 4a presents the relaxed structures of NH₃ adsorbed on monolayer MoS₂ for both pristine and the four types of defective surfaces. To determine the most favorable adsorption site on pristine MoS₂, we consider three possible binding sites: the “hollow” site at the center of a hexagonal ring (labeled “H”), and two on-top sites above Mo (labeled T_m) and S (labeled T_s) atoms. Additionally, two molecular orientations were evaluated—NH₃ pointing “up” (hydrogens away from the surface) and “down” (hydrogens facing the surface). We find that the on-top site with the NH₃ molecule in the up orientation corresponds to the minimum energy configuration, with the hollow-up configuration being slightly less favorable by ~15 meV. In the absence of defects, NH₃ is only weakly physisorbed on the MoS₂ surface, with binding energies ranging from 20 meV to 36 meV. For the defective structures, we focused on NH₃ adsorption at the defect site with the molecule oriented down toward the surface. Except for the V_{MoS3} site, NH₃ exhibits strong chemisorption at the defect sites, with binding energies ranging from 0.9 eV (V_{S3}) to 1.4 eV (V_S). In the V_S structure, NH₃ undergoes dissociation upon absorption, forming an NH fragment that bonds to the vacancy site through a Mo-N bond, while the remaining two hydrogen atoms remain unbound above the surface. In the V_{S3} case, NH₃ dissociates into an NH₂ species bonded to the vacancy site through a Mo-N bond and a hydrogen atom bound to an adjacent S atom. These results are consistent with previous experimental observations indicating that defect sites—particularly sulfur vacancies—are required to facilitate NH₃ chemisorption,³⁷ indicating that desulfurization is a prerequisite for MoN

synthesis from MoS₂ precursors. Figure 4b plots the computed layer dependence of the binding energies for all structures considered. The result shows negligible variation in adsorption energy across different MoS₂ thicknesses, regardless of defect type. The pristine MoS₂ and V_{MoS3} across all layers exhibit weak physisorption with binding energies of 20–36 meV and ~130 meV, respectively. In contrast, the V_s structure binds NH₃ most strongly across all layers (–1.40 eV), followed by V_{MoS3, H} (–1.13 eV) and V_{S3} (–0.90 eV to –1.08 eV). These results clearly indicate that the layer-dependent chemical reactivity observed experimentally cannot be attributed to differences in NH₃ binding energy. Instead, it is more likely governed by the extent of rearrangement of Mo atoms necessary to form the thermodynamically stable MoN phases, as discussed in the preceding sections.

Conclusion

In conclusion, we have systematically investigated the layer-dependent chemical reactivity of MoS₂ in a nitridation reaction, revealing that the energy cost of Mo atom rearrangement governs the observed trend. Monolayer MoS₂ exhibits striking inertness due to high kinetic barriers from significant out-of-plane Mo migration during phase transformation. This leads to distinct morphologies: monolayer and bilayer MoS₂ form discontinuous MoN nanonetworks with many voids, whereas thicker layers yield more continuous and uniform MoN films. The effect also strongly impacts the local conductance of the resulting thin films. DFT calculations reveal that the transformation is driven by desulfurization and strong Mo–N bond formation, while ruling out NH₃ binding as a factor in the layer-dependent reactivity. This work uncovers the atomic-scale mechanisms controlling chemical reactivity and morphology, providing a foundation for tailoring 2D material chemistry in future applications.

Supporting Information

Details for the sample preparation, Raman and PL spectra of MoS₂ with different number of layers, XPS characterizations, TEM and MIM characterizations, MoN coverage calculations, NH₃ absorption energy calculations, additional optical images, statistical analysis on Raman maps, MIM images and TEM images.

Author Information

Corresponding Author

Xi Ling - Department of Chemistry, Division of Materials Science and Engineering, and The Photonics Center, Boston University, Boston, Massachusetts 02215, United States

Email: xiling@bu.edu

Authors

Zifan Wang - Department of Chemistry, Boston University, Boston, Massachusetts 02215, United States

Jiaxuan Wen - Department of Physics, The University of Texas at Austin, Austin, Texas 78712, United States

Tina Mihm - Department of Electrical and Computer Engineering, Boston University, Boston, Massachusetts 02215, United States

Shaopeng Feng - Department of Physics, The University of Texas at Austin, Austin, Texas 78712, United States

Kelvin Huang - Department of Electrical and Computer Engineering, Boston University, Boston, Massachusetts 02215, United States

Jing Tang - Division of Materials Science and Engineering, Boston University, Boston, Massachusetts 02215, United States

Tianshu Li - Division of Materials Science and Engineering, Boston University, Boston, Massachusetts 02215, United States

Liangbo Liang - Center for Nanophase Materials Sciences, Oak Ridge National Laboratory, Oak Ridge, Tennessee 37831, United States.

Sahar Sharifzadeh - Department of Electrical and Computer Engineering, Boston University, Boston, Massachusetts 02215, United States

Keji Lai - Department of Physics, The University of Texas at Austin, Austin, Texas 78712, United States

Notes

The authors declare no competing financial interests.

Acknowledgements

Research is primarily supported by the U.S. Department of Energy (DOE), Office of Science, Basic Energy Sciences (BES), under Award DE-SC0021064. Work by X.L. was also supported by the National Science Foundation (NSF) under Grant Nos. (1945364) and (2111160). The microwave microscopy work (J.W., S.F., K.L.) was supported by the Welch Foundation (Grant No. F-1814). K.L. was also supported by NSF under Grant DMR-2426989. Computational studies by T.M, K.H, and S.S. were supported by DOE BES under Award number DE-SC0023402. L.L. acknowledges work at the Center for Nanophase Materials Sciences, which is a U.S. Department of Energy Office of Science User Facility. This work was performed in part at the Harvard University Center for Nanoscale Systems (CNS), a member of the National Nanotechnology Coordinated Infrastructure Network (NNCI), which is supported by the National Science Foundation under NSF award no. ECCS-2025158. We would like to acknowledge computational resources from the National Energy Research Scientific Computing Center (NERSC), a DOE Office of Science User Facility supported by the Office of Science of the U.S. Department of Energy under Contract No. DE-AC02-05CH11231, and Boston University's Research Computing Services.

References

- (1) Zhang, L.; Wang, N.; Li, Y. Design, Synthesis, and Application of Some Two-Dimensional Materials. *Chem Sci* **2023**, *14* (20), 5266–5290. <https://doi.org/10.1039/D3SC00487B>.
- (2) He, M.; Swager, T. M. Aryl Migration on Graphene. *J Am Chem Soc* **2020**, *142* (42), 17876–17880. <https://doi.org/10.1021/jacs.0c05965>.
- (3) Ding, H.; Li, Y.; Li, M.; Chen, K.; Liang, K.; Chen, G.; Lu, J.; Palisaitis, J.; Persson, P. O. Å.; Eklund, P.; Hultman, L.; Du, S.; Chai, Z.; Gogotsi, Y.; Huang, Q. Chemical Scissor-Mediated Structural Editing of Layered Transition Metal Carbides. *Science (1979)* **2023**, *379* (6637), 1130–1135. <https://doi.org/10.1126/science.add5901>.
- (4) Su, J.; Li, J.; Guo, N.; Peng, X.; Yin, J.; Wang, J.; Lyu, P.; Luo, Z.; Mouthaan, K.; Wu, J.; Zhang, C.; Wang, X.; Lu, J. Intelligent Synthesis of Magnetic Nanographenes via Chemist-Intuited Atomic Robotic Probe. *Nature Synthesis* **2024**, *3* (4), 466–476. <https://doi.org/10.1038/s44160-024-00488-7>.

- (5) Lyu, B.; Chen, J.; Wang, S.; Lou, S.; Shen, P.; Xie, J.; Qiu, L.; Mitchell, I.; Li, C.; Hu, C.; Zhou, X.; Watanabe, K.; Taniguchi, T.; Wang, X.; Jia, J.; Liang, Q.; Chen, G.; Li, T.; Wang, S.; Ouyang, W.; Hod, O.; Ding, F.; Urbakh, M.; Shi, Z. Graphene Nanoribbons Grown in HBN Stacks for High-Performance Electronics. *Nature* **2024**, 628 (8009), 758–764. <https://doi.org/10.1038/s41586-024-07243-0>.
- (6) Zhao, J.; Li, L.; Li, P.; Dai, L.; Dong, J.; Zhou, L.; Wang, Y.; Zhang, P.; Ji, K.; Zhang, Y.; Yu, H.; Wei, Z.; Li, J.; Li, X.; Huang, Z.; Wang, B.; Liu, J.; Chen, Y.; Zhang, X.; Wang, S.; Li, N.; Yang, W.; Shi, D.; Pan, J.; Du, S.; Du, L.; Zhang, G. Realization of 2D Metals at the Ångström Thickness Limit. *Nature* **2025**, 639 (8054), 354–359. <https://doi.org/10.1038/s41586-025-08711-x>.
- (7) Wang, C.; Jing, Y.; Zhu, D.; Xin, H. L. Atomic Origin of Chemomechanical Failure of Layered Cathodes in All-Solid-State Batteries. *J Am Chem Soc* **2024**, 146 (26), 17712–17718. <https://doi.org/10.1021/jacs.4c02198>.
- (8) Ge, X.; Yin, J.; Ren, Z.; Yan, K.; Jing, Y.; Cao, Y.; Fei, N.; Liu, X.; Wang, X.; Zhou, X.; Chen, L.; Yuan, W.; Duan, X. Atomic Design of Alkyne Semihydrogenation Catalysts via Active Learning. *J Am Chem Soc* **2024**, 146 (7), 4993–5004. <https://doi.org/10.1021/jacs.3c14495>.
- (9) Liao, L.; Wang, H.; Peng, H.; Yin, J.; Koh, A. L.; Chen, Y.; Xie, Q.; Peng, H.; Liu, Z. Van Hove Singularity Enhanced Photochemical Reactivity of Twisted Bilayer Graphene. *Nano Lett* **2015**, 15 (8), 5585–5589. <https://doi.org/10.1021/acs.nanolett.5b02240>.
- (10) Abraham, J.; Vasu, K. S.; Williams, C. D.; Gopinadhan, K.; Su, Y.; Cherian, C. T.; Dix, J.; Prestat, E.; Haigh, S. J.; Grigorieva, I. V.; Carbone, P.; Geim, A. K.; Nair, R. R. Tunable Sieving of Ions Using Graphene Oxide Membranes. *Nat Nanotechnol* **2017**, 12 (6), 546–550. <https://doi.org/10.1038/nnano.2017.21>.
- (11) Xie, L.; Wang, L.; Zhao, W.; Liu, S.; Huang, W.; Zhao, Q. WS₂ Moiré Superlattices Derived from Mechanical Flexibility for Hydrogen Evolution Reaction. *Nat Commun* **2021**, 12 (1), 5070. <https://doi.org/10.1038/s41467-021-25381-1>.
- (12) Zhang, K.; Yu, Y.; Carr, S.; Babar, M.; Zhu, Z.; Kim, B. J.; Groschner, C.; Khaloo, N.; Taniguchi, T.; Watanabe, K.; Viswanathan, V.; Bediako, D. K. Anomalous Interfacial Electron-Transfer Kinetics in Twisted Trilayer Graphene Caused by Layer-Specific Localization. *ACS Cent Sci* **2023**, 9 (6), 1119–1128. <https://doi.org/10.1021/acscentsci.3c00326>.
- (13) Zhang, Y.; Yuan, N. F. Q.; Fu, L. Moiré Quantum Chemistry: Charge Transfer in Transition Metal Dichalcogenide Superlattices. *Phys Rev B* **2020**, 102 (20), 201115. <https://doi.org/10.1103/PhysRevB.102.201115>.
- (14) Zhang, Y.; Felser, C.; Fu, L. Moiré Metal for Catalysis. *Phys Rev B* **2024**, 110 (4), L041407. <https://doi.org/10.1103/PhysRevB.110.L041407>.

- (15) Xu, X.; Wang, X.; Jiang, D. Band Gap as a Novel Descriptor for the Reactivity of 2D Titanium Dioxide and Its Supported Pt Single Atom for Methane Activation. *J Phys Chem Lett* **2021**, *12* (10), 2484–2488. <https://doi.org/10.1021/acs.jpcclett.1c00318>.
- (16) Wu, Y.; Wang, J.; Li, Y.; Zhou, J.; Wang, B. Y.; Yang, A.; Wang, L.-W.; Hwang, H. Y.; Cui, Y. Observation of an Intermediate State during Lithium Intercalation of Twisted Bilayer MoS₂. *Nat Commun* **2022**, *13* (1), 3008. <https://doi.org/10.1038/s41467-022-30516-z>.
- (17) Banerjee, S.; Rappe, A. M. Mechanochemical Molecular Migration on Graphene. *J Am Chem Soc* **2022**, *144* (16), 7181–7188. <https://doi.org/10.1021/jacs.1c13193>.
- (18) Wang, X.; Fan, W.; Fan, Z.; Dai, W.; Zhu, K.; Hong, S.; Sun, Y.; Wu, J.; Liu, K. Substrate Modified Thermal Stability of Mono- and Few-Layer MoS₂. *Nanoscale* **2018**, *10* (7), 3540–3546. <https://doi.org/10.1039/C7NR08941D>.
- (19) Voiry, D.; Goswami, A.; Kappera, R.; Silva, C. de C. C. e; Kaplan, D.; Fujita, T.; Chen, M.; Asefa, T.; Chhowalla, M. Covalent Functionalization of Monolayered Transition Metal Dichalcogenides by Phase Engineering. *Nat Chem* **2015**, *7* (1), 45–49. <https://doi.org/10.1038/nchem.2108>.
- (20) Chen, X.; Bartlam, C.; Lloret, V.; Moses Badlyan, N.; Wolff, S.; Gillen, R.; Stimpel-Lindner, T.; Maultzsch, J.; Duesberg, G. S.; Knirsch, K. C.; Hirsch, A. Covalent Bisfunctionalization of Two-Dimensional Molybdenum Disulfide. *Angewandte Chemie International Edition* **2021**, *60* (24), 13484–13492. <https://doi.org/10.1002/anie.202103353>.
- (21) Sun, L.; Yan, X.; Zheng, J.; Yu, H.; Lu, Z.; Gao, S.; Liu, L.; Pan, X.; Wang, D.; Wang, Z.; Wang, P.; Jiao, L. Layer-Dependent Chemically Induced Phase Transition of Two-Dimensional MoS₂. *Nano Lett* **2018**, *18* (6), 3435–3440. <https://doi.org/10.1021/acs.nanolett.8b00452>.
- (22) Yu, Y.; Huang, S.-Y.; Li, Y.; Steinmann, S. N.; Yang, W.; Cao, L. Layer-Dependent Electrocatalysis of MoS₂ for Hydrogen Evolution. *Nano Lett* **2014**, *14* (2), 553–558. <https://doi.org/10.1021/nl403620g>.
- (23) Zhou, L.; Zhou, L.; Yang, M.; Wu, D.; Liao, L.; Yan, K.; Xie, Q.; Liu, Z.; Peng, H.; Liu, Z. Free Radical Reactions in Two Dimensions: A Case Study on Photochlorination of Graphene. *Small* **2013**, *9* (8), 1388–1396. <https://doi.org/10.1002/smll.201202969>.
- (24) Ding, Y.; Peng, Q.; Gan, L.; Wu, R.; Ou, X.; Zhang, Q.; Luo, Z. Stacking-Mode-Induced Reactivity Enhancement for Twisted Bilayer Graphene. *Chemistry of Materials* **2016**, *28* (4), 1034–1039. <https://doi.org/10.1021/acs.chemmater.5b04002>.

- (25) Bard, A. J. & F. L. R. *Electrochemical Methods: Fundamentals and Applications* 2nd Edn. *Russian Journal of Electrochemistry* **2002**, *38* (12), 1364–1365. <https://doi.org/10.1023/A:1021637209564>.
- (26) Schmickler, W.; Santos, E. *Interfacial Electrochemistry 2nd Edn*; Springer Berlin Heidelberg: Berlin, Heidelberg, 2010. <https://doi.org/10.1007/978-3-642-04937-8>.
- (27) Henstridge, M. C.; Laborda, E.; Rees, N. V.; Compton, R. G. Marcus–Hush–Chidsey Theory of Electron Transfer Applied to Voltammetry: A Review. *Electrochim Acta* **2012**, *84*, 12–20. <https://doi.org/10.1016/j.electacta.2011.10.026>.
- (28) Kurchin, R.; Viswanathan, V. Marcus–Hush–Chidsey Kinetics at Electrode–Electrolyte Interfaces. *J Chem Phys* **2020**, *153* (13). <https://doi.org/10.1063/5.0023611>.
- (29) Nair, N.; Kim, W.-J.; Usrey, M. L.; Strano, M. S. A Structure–Reactivity Relationship for Single Walled Carbon Nanotubes Reacting with 4-Hydroxybenzene Diazonium Salt. *J Am Chem Soc* **2007**, *129* (13), 3946–3954. <https://doi.org/10.1021/ja068018i>.
- (30) Sharma, R.; Baik, J. H.; Perera, C. J.; Strano, M. S. Anomalous Large Reactivity of Single Graphene Layers and Edges toward Electron Transfer Chemistries. *Nano Lett* **2010**, *10* (2), 398–405. <https://doi.org/10.1021/nl902741x>.
- (31) Sharma, R.; Nair, N.; Strano, M. S. Structure–Reactivity Relationships for Graphene Nanoribbons. *The Journal of Physical Chemistry C* **2009**, *113* (33), 14771–14777. <https://doi.org/10.1021/jp904814h>.
- (32) Heller, I.; Kong, J.; Williams, K. A.; Dekker, C.; Lemay, S. G. Electrochemistry at Single-Walled Carbon Nanotubes: The Role of Band Structure and Quantum Capacitance. *J Am Chem Soc* **2006**, *128* (22), 7353–7359. <https://doi.org/10.1021/ja061212k>.
- (33) Yu, Y.; Zhang, K.; Parks, H.; Babar, M.; Carr, S.; Craig, I. M.; Van Winkle, M.; Lyssenko, A.; Taniguchi, T.; Watanabe, K.; Viswanathan, V.; Bediako, D. K. Tunable Angle-Dependent Electrochemistry at Twisted Bilayer Graphene with Moiré Flat Bands. *Nat Chem* **2022**, *14* (3), 267–273. <https://doi.org/10.1038/s41557-021-00865-1>.
- (34) Wang, Q. H.; Jin, Z.; Kim, K. K.; Hilmer, A. J.; Paulus, G. L. C.; Shih, C.-J.; Ham, M.-H.; Sanchez-Yamagishi, J. D.; Watanabe, K.; Taniguchi, T.; Kong, J.; Jarillo-Herrero, P.; Strano, M. S. Understanding and Controlling the Substrate Effect on Graphene Electron-Transfer Chemistry via Reactivity Imprint Lithography. *Nat Chem* **2012**, *4* (9), 724–732. <https://doi.org/10.1038/nchem.1421>.
- (35) Cao, J.; Li, T.; Gao, H.; Lin, Y.; Wang, X.; Wang, H.; Palacios, T.; Ling, X. Realization of 2D Crystalline Metal Nitrides via Selective Atomic Substitution. *Sci Adv* **2020**, *6* (2). <https://doi.org/10.1126/sciadv.aax8784>.

- (36) Gao, H.; Cao, J.; Li, T.; Luo, W.; Gray, M.; Kumar, N.; Burch, K. S.; Ling, X. Phase-Controllable Synthesis of Ultrathin Molybdenum Nitride Crystals Via Atomic Substitution of MoS₂. *Chemistry of Materials* **2022**, *34* (1), 351–357. <https://doi.org/10.1021/acs.chemmater.1c03712>.
- (37) Li, T.; Cao, J.; Gao, H.; Wang, Z.; Geiwitz, M.; Burch, K. S.; Ling, X. Epitaxial Atomic Substitution for MoS₂-MoN Heterostructure Synthesis. *ACS Appl Mater Interfaces* **2022**. <https://doi.org/10.1021/acsami.2c16425>.
- (38) Yao, C.-H.; Gao, H.; Ping, L.; Gulo, D. P.; Liu, H.-L.; Tuan Hung, N.; Saito, R.; Ling, X. Nontrivial Raman Characteristics in 2D Non-Van Der Waals Mo₅N₆. *ACS Nano* **2024**, *18* (47), 32458–32467. <https://doi.org/10.1021/acs.nano.4c06250>.
- (39) Rice, C.; Young, R. J.; Zan, R.; Bangert, U.; Wolverson, D.; Georgiou, T.; Jalil, R.; Novoselov, K. S. Raman-Scattering Measurements and First-Principles Calculations of Strain-Induced Phonon Shifts in Monolayer MoS₂. *Phys Rev B* **2013**, *87* (8), 081307. <https://doi.org/10.1103/PhysRevB.87.081307>.
- (40) Zhu, C. R.; Wang, G.; Liu, B. L.; Marie, X.; Qiao, X. F.; Zhang, X.; Wu, X. X.; Fan, H.; Tan, P. H.; Amand, T.; Urbaszek, B. Strain Tuning of Optical Emission Energy and Polarization in Monolayer and Bilayer MoS₂. *Phys Rev B* **2013**, *88* (12), 121301. <https://doi.org/10.1103/PhysRevB.88.121301>.
- (41) Conley, H. J.; Wang, B.; Ziegler, J. I.; Haglund, R. F.; Pantelides, S. T.; Bolotin, K. I. Bandgap Engineering of Strained Monolayer and Bilayer MoS₂. *Nano Lett* **2013**, *13* (8), 3626–3630. <https://doi.org/10.1021/nl4014748>.
- (42) Li, H.; Zhang, Q.; Yap, C. C. R.; Tay, B. K.; Edwin, T. H. T.; Olivier, A.; Baillargeat, D. From Bulk to Monolayer MoS₂: Evolution of Raman Scattering. *Adv Funct Mater* **2012**, *22* (7), 1385–1390. <https://doi.org/10.1002/adfm.201102111>.
- (43) Mak, K. F.; Lee, C.; Hone, J.; Shan, J.; Heinz, T. F. Atomically Thin MoS₂: A New Direct-Gap Semiconductor. *Phys Rev Lett* **2010**, *105* (13), 136805. <https://doi.org/10.1103/PhysRevLett.105.136805>.
- (44) Splendiani, A.; Sun, L.; Zhang, Y.; Li, T.; Kim, J.; Chim, C.-Y.; Galli, G.; Wang, F. Emerging Photoluminescence in Monolayer MoS₂. *Nano Lett* **2010**, *10* (4), 1271–1275. <https://doi.org/10.1021/nl903868w>.
- (45) Lai, K.; Kundhikanjana, W.; Kelly, M. A.; Shen, Z.-X. Nanoscale Microwave Microscopy Using Shielded Cantilever Probes. *Appl Nanosci* **2011**, *1* (1), 13–18. <https://doi.org/10.1007/s13204-011-0002-7>.
- (46) Chu, Z.; Zheng, L.; Lai, K. Microwave Microscopy and Its Applications. *Annu Rev Mater Res* **2020**, *50* (1), 105–130. <https://doi.org/10.1146/annurev-matsci-081519-011844>.

- (47) Wang, Y. Y.; Ni, Z. H.; Shen, Z. X.; Wang, H. M.; Wu, Y. H. Interference Enhancement of Raman Signal of Graphene. *Appl Phys Lett* **2008**, *92* (4). <https://doi.org/10.1063/1.2838745>.
- (48) Yoon, D.; Moon, H.; Son, Y.-W.; Choi, J. S.; Park, B. H.; Cha, Y. H.; Kim, Y. D.; Cheong, H. Interference Effect on Raman Spectrum of Graphene on SiO₂/Si. *Phys Rev B* **2009**, *80* (12), 125422. <https://doi.org/10.1103/PhysRevB.80.125422>.
- (49) Li, S.-L.; Miyazaki, H.; Song, H.; Kuramochi, H.; Nakaharai, S.; Tsukagoshi, K. Quantitative Raman Spectrum and Reliable Thickness Identification for Atomic Layers on Insulating Substrates. *ACS Nano* **2012**, *6* (8), 7381–7388. <https://doi.org/10.1021/nn3025173>.
- (50) Splendiani, A.; Sun, L.; Zhang, Y.; Li, T.; Kim, J.; Chim, C.-Y.; Galli, G.; Wang, F. Emerging Photoluminescence in Monolayer MoS₂. *Nano Lett* **2010**, *10* (4), 1271–1275. <https://doi.org/10.1021/nl903868w>.
- (51) Bull, C. L.; McMillan, P. F.; Soignard, E.; Leinenweber, K. Determination of the Crystal Structure of δ -MoN by Neutron Diffraction. *J Solid State Chem* **2004**, *177* (4–5), 1488–1492. <https://doi.org/10.1016/j.jssc.2003.11.033>.
- (52) Ganin, A. Yu.; Kienle, L.; Vajenine, G. V. Synthesis and Characterisation of Hexagonal Molybdenum Nitrides. *J Solid State Chem* **2006**, *179* (8), 2339–2348. <https://doi.org/10.1016/j.jssc.2006.05.025>.
- (53) Wang, S.; Antonio, D.; Yu, X.; Zhang, J.; Cornelius, A. L.; He, D.; Zhao, Y. The Hardest Superconducting Metal Nitride. *Sci Rep* **2015**, *5* (1), 13733. <https://doi.org/10.1038/srep13733>.
- (54) Jauberteau, I.; Bessaoudou, A.; Mayet, R.; Cornette, J.; Jauberteau, J.; Carles, P.; Merle-Méjean, T. Molybdenum Nitride Films: Crystal Structures, Synthesis, Mechanical, Electrical and Some Other Properties. *Coatings* **2015**, *5* (4), 656–687. <https://doi.org/10.3390/coatings5040656>.
- (55) Sun, G.; Zhang, G.; Chou, K. Synthesis of Molybdenum Nitrides Nanosheets by Nitriding 2H-MoS₂ with Ammonia. *Journal of the American Ceramic Society* **2018**, *101* (7), 2796–2808. <https://doi.org/10.1111/jace.15467>.
- (56) Guy, K.; Tessier, F.; Kaper, H.; Grasset, F.; Dumait, N.; Demange, V.; Nishio, M.; Matsushita, Y.; Matsui, Y.; Takei, T.; Lechevalier, D.; Tardivat, C.; Uchikoshi, T.; Ohashi, N.; Cordier, S. Original Synthesis of Molybdenum Nitrides Using Metal Cluster Compounds as Precursors: Applications in Heterogeneous Catalysis. *Chemistry of Materials* **2020**, *32* (14), 6026–6034. <https://doi.org/10.1021/acs.chemmater.0c01369>.
- (57) Jaf, Z. N.; Miran, H. A.; Jiang, Z.-T.; Altarawneh, M. Molybdenum Nitrides from Structures to Industrial Applications. *Reviews in Chemical Engineering* **2023**, *39* (3), 329–361. <https://doi.org/10.1515/revce-2021-0002>.

- (58) Inani, H.; Shin, D. H.; Madsen, J.; Jeong, H.; Kwon, M. H.; McEvoy, N.; Susi, T.; Mangler, C.; Lee, S. W.; Mustonen, K.; Kotakoski, J. Step-By-Step Atomic Insights into Structural Reordering from 2D to 3D MoS₂. *Adv Funct Mater* **2021**, *31* (13). <https://doi.org/10.1002/adfm.202008395>.
- (59) Arunachalam, H. N.; Perarasan, T.; Durairaj, S.; Sinha, J.; Eswaran, S. K.; Chandramohan, S.; Tripathi, J. K. Evolutions of 3D MoS₂ Nano-Islands on Monolayer MoS₂ Edges under Low-Energy Ion Irradiation. *J Mater Sci* **2025**, *60* (8), 3863–3879. <https://doi.org/10.1007/s10853-025-10683-2>.
- (60) Hong, J.; Hu, Z.; Probert, M.; Li, K.; Lv, D.; Yang, X.; Gu, L.; Mao, N.; Feng, Q.; Xie, L.; Zhang, J.; Wu, D.; Zhang, Z.; Jin, C.; Ji, W.; Zhang, X.; Yuan, J.; Zhang, Z. Exploring Atomic Defects in Molybdenum Disulphide Monolayers. *Nat Commun* **2015**, *6* (1), 6293. <https://doi.org/10.1038/ncomms7293>.

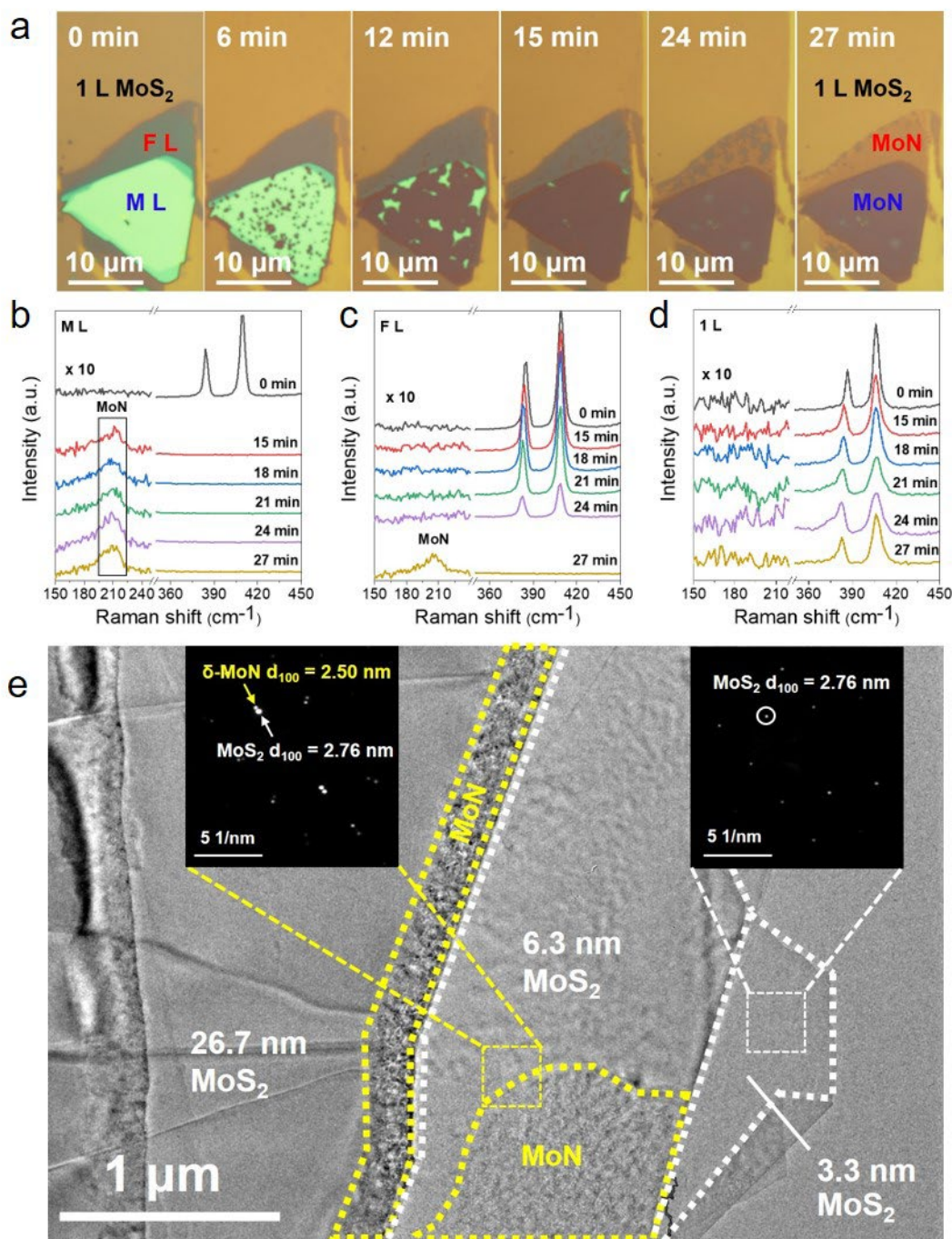


Figure 1. Demonstration of the chemical reactivity differences among 1L, FL and ML MoS₂. (a) Optical images of a step-shaped MoS₂ flake at various stages of the nitridation atomic substitution reaction. (b-d) Corresponding Raman spectra measured in the ML (b), FL (c) and 1L region (d) of the MoS₂ flakes in (a). (e) TEM image of a partially converted step-shaped MoS₂. Thickness step edges between regions of different layer numbers are indicated by white dashed lines, while areas converted to MoN are outlined in yellow. Insets are SAED patterns acquired from the marked locations.

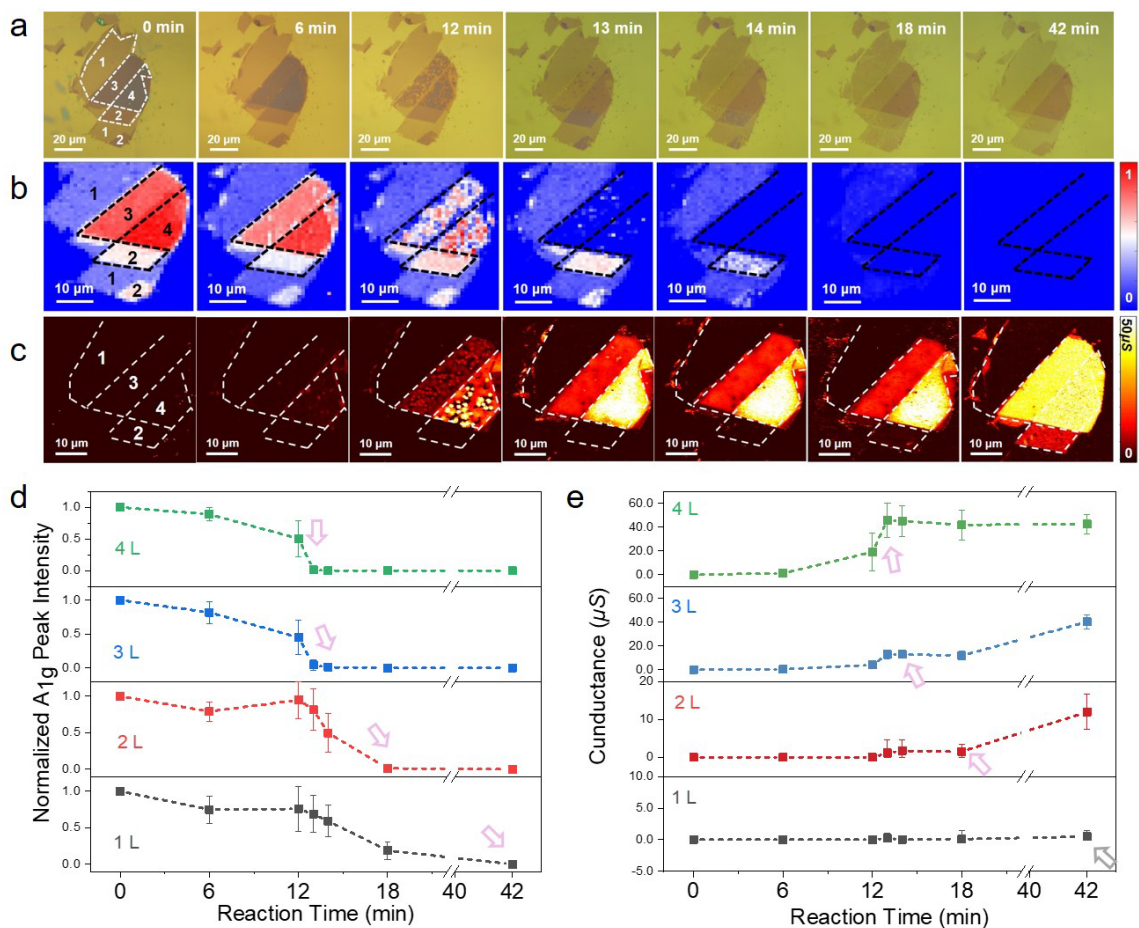


Figure 2. Investigation of the layered-dependent chemical reactivity on ultrathin MoS₂ ranging from 1L to 4L. (a) Optical images, (b) Raman intensity maps of the A_{1g} mode of MoS₂, (c) conductance maps from the MIM measurements of an ultrathin step-shaped MoS₂ flake at different conversion stages. The 1L, 2L, 3L and 4L regions are labeled as 1, 2, 3 and 4, respectively. Boundaries between adjacent thickness regions are indicated by white dashed lines. (d) Time-dependent evolution of the average A_{1g} peak intensity extracted from the Raman maps shown in (b). The average A_{1g} intensity is normalized to its initial value prior to the reaction. (e) Time-dependent evolution of the average sheet conductance values extracted from the maps shown in (c). The pink arrows indicate the shift in the duration required to complete the conversion, as inferred from changes in both Raman intensity and electrical conductance. The gray arrow in (e) marks a hypothetical point where conductance increase would occur in the 1L sample.

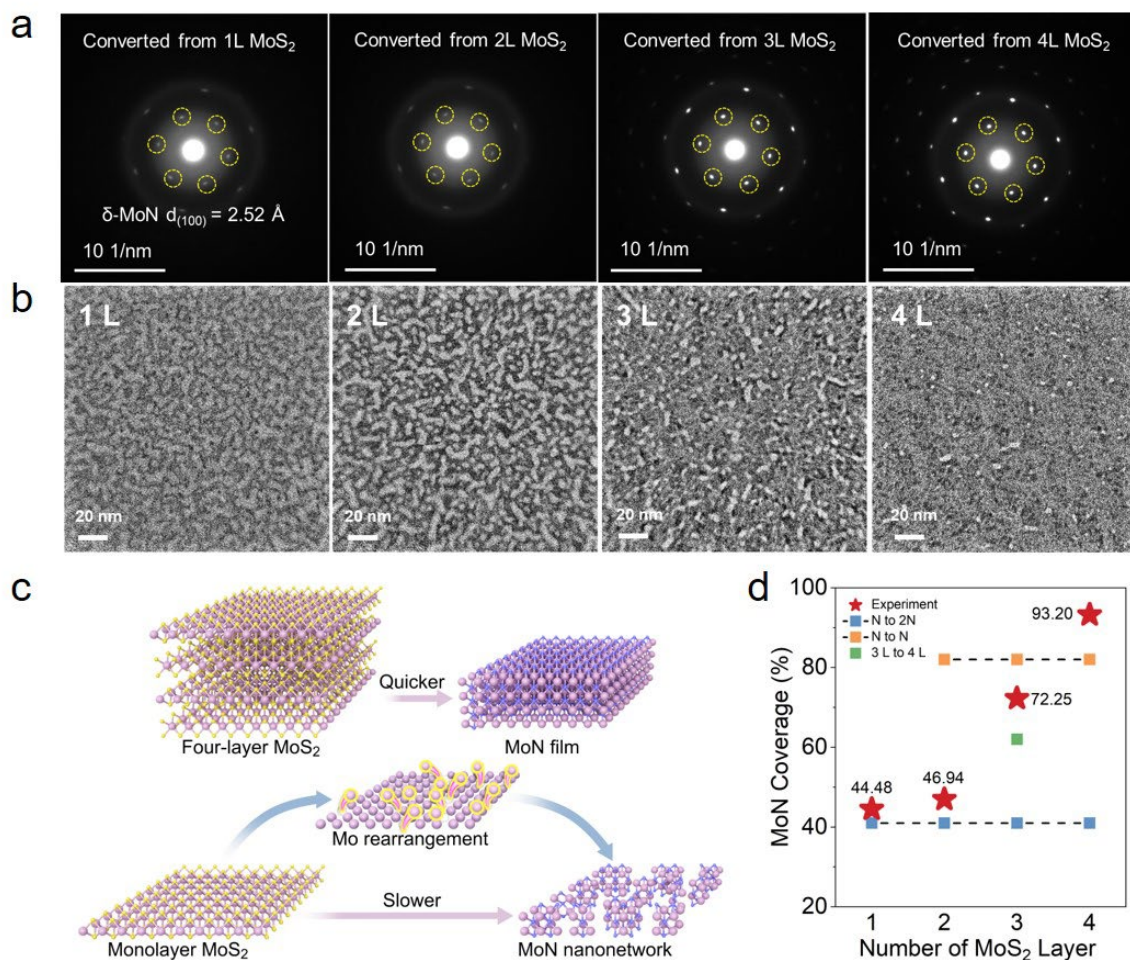


Figure 3. Structural and morphological analysis of MoN formed from the nitridation of 1L to 4L MoS₂, and the proposed structural transformation pathways. (a) SAED patterns and (b) TEM images of MoN crystals from 1L, 2L, 3L, and 4L MoS₂, respectively. (c) Schematic illustration of the distinct structural transformation pathways from 1L and 4L MoS₂ to their corresponding MoN structures. (d) MoN film coverages obtained experimentally (star symbols) and theoretically (square symbols) from the conversion of 1L to 4L MoS₂.

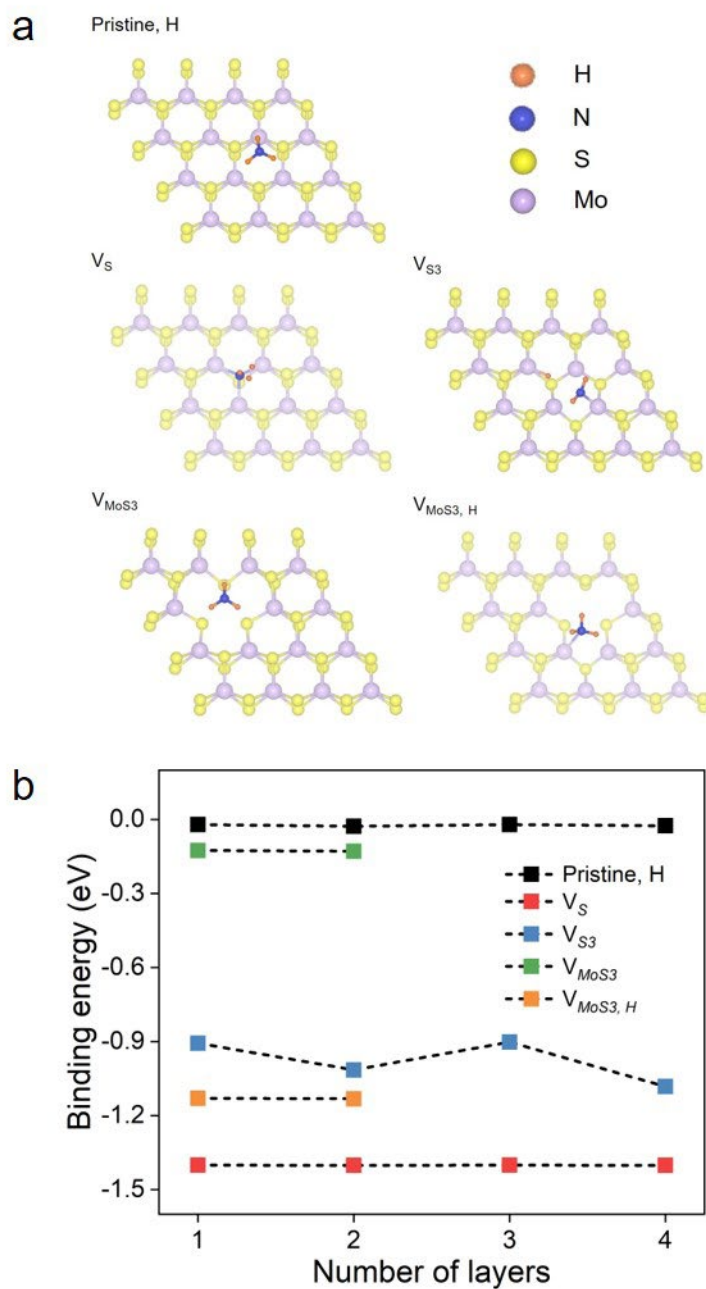


Figure 4. Structures and binding energies of NH_3 adsorbed on pristine and defective MoS_2 surfaces with varying layer numbers. (a) The optimized structure for a NH_3 molecule adsorbed on monolayer MoS_2 . (b) Variation of NH_3 binding energy with increasing number of MoS_2 layers.

Supplementary Materials for

**Mo Atom Rearrangement Drives Layer-Dependent Reactivity in Two-Dimensional
MoS₂**

Zifan Wang¹, Jiaxuan Wen², Tina Mihm³, Shaopeng Feng², Kelvin Huang³, Jing Tang⁴,
Tianshu Li⁴, Liangbo Liang⁶, Sahar Sharifzadeh³, Keji Lai², Xi Ling^{1, 4, 5*}

¹ Department of Chemistry, Boston University, Boston, Massachusetts 02215, USA.

² Department of Physics, The University of Texas at Austin, Austin, Texas 78712, USA.

³ Department of Electrical and Computer Engineering, Boston University, Boston, Massachusetts 02215, USA.

⁴ Division of Materials Science and Engineering, Boston University, Boston, Massachusetts 02215, USA.

⁵ The Photonics Center, Boston University, Boston, Massachusetts 02215, USA.

⁶ Center for Nanophase Materials Sciences, Oak Ridge National Laboratory, Oak Ridge, Tennessee 37831, USA.

*To whom the correspondence should be addressed. Email address: xiling@bu.edu

Methods

Nitridation Atomic Substitution Reaction of MoS₂

MoS₂ flakes were prepared via mechanical exfoliation of bulk single crystals and transferred onto substrates such as SiO₂/Si. The sample were then loaded into a 1-inch quartz tube housed within a tube furnace. For the atomic substitution reaction, the furnace temperature was ramped to 650 °C at a rate of 45 °C/min and held at the target temperature for various durations for the reaction. A mixture of NH₃ gas and argon was introduced into the system as the nitrogen source for the atomic substitution. The flow rate of each gas is 50 sccm. After the reaction, the furnace was cooled naturally to room temperature before retrieving the samples for subsequent characterization using various analytical techniques.

TEM Sample Preparation and Characterization

MoS₂ flakes of interest are transferred from the SiO₂/Si substrate onto silicon nitride TEM grids via a dry-transfer method. Specifically, a drop of polystyrene (PS) in toluene (20% wt) is casted and spin coated on the SiO₂/Si substrate containing the target MoS₂ flake. The substrate is then heated on a hot plate at 85 °C for 4 mins, followed by immersion in deionized (DI) water for 5 mins. Subsequently, the PS film—along with the embedded MoS₂ flake—is lifted from the substrate using tweezers and transferred onto a polydimethylsiloxane (PDMS) stamp, with the flake-oriented face-up. The PDMS stamp is then brought into contact with the TEM grid and heated at 95 °C for 10 minutes, during which the PS film and MoS₂ flake detach from the PDMS and adhere to the grid. To remove the PS film, the TEM grid is soaked in toluene for 20 minutes. Finally, a 90-minute nitridation reaction at temperature of 680 °C is performed to fully convert the MoS₂ flake to MoN. TEM measurements are performed on JEOL ARM 200F STEM in the Center for Nanoscale Systems (CNS) at Harvard University.

Raman and Photoluminescence (PL) Measurements

Raman and PL measurements were performed using a Renishaw inVia Raman microscope equipped with a 532 nm laser excitation. Raman mappings were performed over an area of $40\ \mu\text{m} \times 48\ \mu\text{m}$ at various stages of the conversion process, with a step size of $1\ \mu\text{m}$ for both X-axis and Y-axis. In order to account for potential variations in signal intensity, Raman measurements were also acquired from a reference SiO_2/Si substrate. The intensity of the Si peak at $520\ \text{cm}^{-1}$ from the reference substrate is denoted as $I_{\text{Si-Xmin}}$, where X presents the reaction time in min. Calibration and normalization were then applied to each point in all Raman maps using the following equation:

$$I_{\text{C-Xmin}} = I \times (I_{\text{Si-0min}} / I_{\text{Si-Xmin}})$$

$$I_{\text{N-Xmin}} = I_{\text{C-Xmin}} / I_{\text{max-0min}}$$

Here, I is the original intensity measured at X min, $I_{\text{C-Xmin}}$ is the calibrated intensity using the reference SiO_2/Si substrate, $I_{\text{max-0min}}$ is the highest intensity value within the map acquired at 0 min, and $I_{\text{N-Xmin}}$ is the normalized intensity to the calibrated intensity value at 0 min. The average and standard deviation of $I_{\text{N-Xmin}}$ in each of the four thickness regions (1L to 4L) were calculated and plotted as a function of the reaction time. The results are presented in Figure S4.

Statistical Analysis of Raman Map

The relative intensity of each point ($I_{\text{R-Xmin}}$) in the Raman maps was calculated using the formula shown below:

$$I_{\text{R-Xmin}} = I_{\text{N-Xmin}} / I_{\text{N-0min}}$$

The average and standard deviation of $I_{\text{R-Xmin}}$ in each of the four thickness regions were

calculated and plotted as a function of the reaction time. The result is presented in Figure 2d.

Microwave Impedance Microscopy (MIM) Measurements and Finite-Element Analysis (FEA)

The MIM experiments in this work were performed on an AFM platform (ParkAFM XE-70) using tapping-mode AFM cantilevers with an overall Au coating (160AC-GG) from OPUS.¹ Before the measurement, the mixer phase was adjusted such that the signal in the MIM-Re channel is zero on the insulating SiO₂ substrate. The measured MIM-Re and MIM-Im images at different stages of the conversion process in Fig. 2 in the main text are shown in Fig.S5(a) and (b), respectively. The commercial software COMSOL 5.4 was used to perform finite element analysis (FEA) to simulate the real and imaginary parts of the admittance for the specific tip-sample geometry in Fig. S5(c). In the experiment, the cantilever tip oscillates sinusoidally with an amplitude of 50 nm and a frequency of 250.7 kHz. As shown in Fig.S5(d), by mapping the tip oscillation onto the MIM approach curve, we can establish the relationship between the actual oscillating signal and time. Applying a Fast Fourier Transform (FFT) to this time-domain signal, we obtain the simulated AC MIM response as a function of sheet conductance in Fig.S5(d). In this study, the simulated ratio of MIM-Re to MIM-Im was calculated and compared with experimental data to form the local sheet conductance images of the MoS₂/MoN sample, as shown in Fig.2c in the main text.

Estimation of MoN Film Coverage from TEM Analysis

Image Processing:

To improve image contrast and correct uneven illumination, Contrast Limited Adaptive Histogram Equalization (CLAHE)² was applied in the CIELAB color space. The original image was first converted from BGR to LAB color space to isolate the luminance channel (L) from the chromatic channels (A and B). CLAHE was applied exclusively to the L

channel using a clip limit of 10 and a tile grid size of 10×10 , allowing for localized contrast enhancement while minimizing noise amplification. The enhanced L channel was then recombined with the original A and B channels to reconstruct the LAB image, which was subsequently converted back to the BGR color space. This method preserves chromatic integrity while effectively correcting spatial variations in lighting.

Coverage Estimation:

To quantitatively estimate the areal coverage of MoN film, the contrast-enhanced image was first converted to grayscale and binarized using a global intensity thresholding method. An empirically determined threshold was applied via the inverse binary thresholding function to distinguish the darker material region (e.g. MoN) from the lighter background (e.g. blank TEM grid region). In the resulting binary image, pixels corresponding to the material were assigned a value of 255 (white), and background pixels were set to 0 (black). The material coverage percentage was then computed as the ratio of material pixels ($N_{material}$) to the total number of pixels in the image (N_{total}), expressed as:

$$Coverage\ Rate = \left(\frac{N_{material}}{N_{total}} \right) * 100\%$$

This approach provides a robust, reproducible means to quantify the surface coverage of materials following contrast enhancement and noise suppression.

Theoretical and Computational Calculations

First-principles density functional theory (DFT) calculations were performed with a planewave basis as implemented in the Vienna Ab-initio Simulation Package (VASP).^{3–7} All calculations were run with VASP 6.4.2 using the Perdew–Burke–Ernzerhof (PBE)⁸ generalized gradient approximation functional to treat the exchange-correlation energy. We employed frozen core projector-augmented wave (PAW) potentials to describe the nuclei and core with default pseudopotentials for VASP.^{9,10} For the unit cell, we utilized a $6 \times 6 \times 1$ k-point mesh with a planewave cutoff of 388 eV, which converged the total

energy below 1 meV/atom. Geometry optimizations were done using the RMM-DIIS^{3,4,11} algorithm, where all atoms were allowed to optimize until all forces were converged to less than 0.01 eV/Å. The lattice vectors kept to that of the unit cell and were not re-optimized for the defective supercells. The lattice vectors of our unit cell were (3.181689, 3.181689, 14.838772) Å, with cell angles of (90°, 90°, 120°).

The NH₃ molecule was adsorbed on the surface of a supercell, with the size of supercell increased as the size of defect was increased. All systems had a 10 Å vacuum layer in the c direction to avoid inter-layer interactions. For the sulfur vacancies (V_s and V_{s3}), a 6 × 6 × *n* supercell was utilized in order to reduce interactions between defect sites, whereas for the V_{MoS3} structure an 8 × 8 × *n* supercell was found to be necessary based on strain analysis at the edge of the supercell. Due to the larger computational cost for V_{MoS3}, we only considered this configuration with 1L and 2L MoS₂. Supercell calculations were performed with a 1 × 1 × 1 k-point mesh for all defect configurations except for V_{s3} 1L and 2L configurations for which we utilized a 2 × 2 × 1 k-point mesh because this k-point mesh was found to be necessary to obtain the lowest energy atomic structure.

The binding energy for an NH₃ molecule adsorbed onto the MoS₂ surface was calculated as,

$$E_{bind} = E_{MoS_2-NH_3} - E_{MoS_2} - E_{NH_3},$$

where $E_{MoS_2-NH_3}$ is the energy of the MoS₂ with the NH₃ on the surface, E_{MoS_2} is the energy of the MoS₂ surface, and E_{NH_3} is the energy of the NH₃ molecule. We note that by this definition a negative E_{bind} indicates binding and positive indicates an unbound molecules.

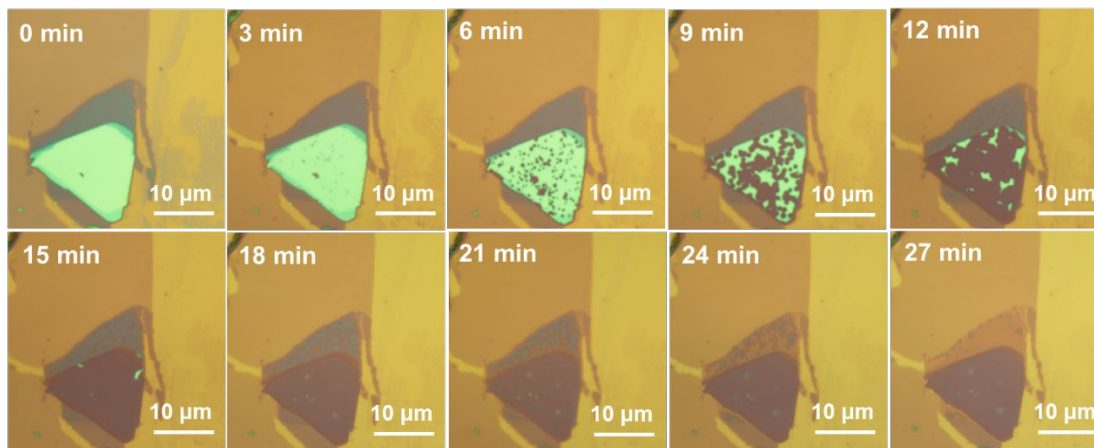


Figure S1. Optical images of the step-shaped MoS₂ at various stages of the nitridation atomic substitution reaction.

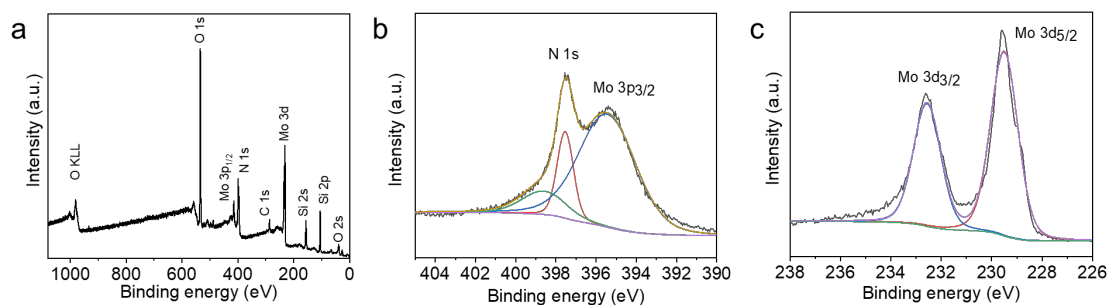


Figure S2. (a) XPS survey spectrum of the fully converted sample. (b-c) Fine scan of the XPS spectrum in the (b) Mo3p and N 1s region and (c) Mo 3d region.

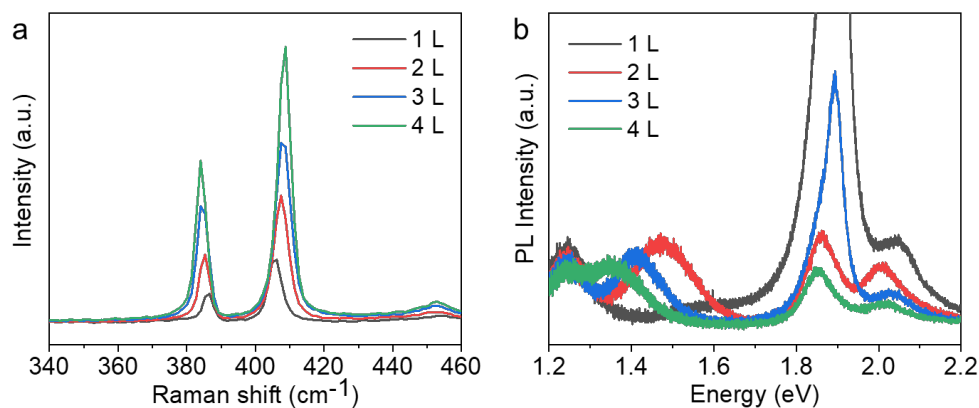


Figure S3. Raman (a) and PL (b) spectra measured at 1L, 2L, 3L and 4L regions of the ultrathin step-shaped MoS₂ sample.

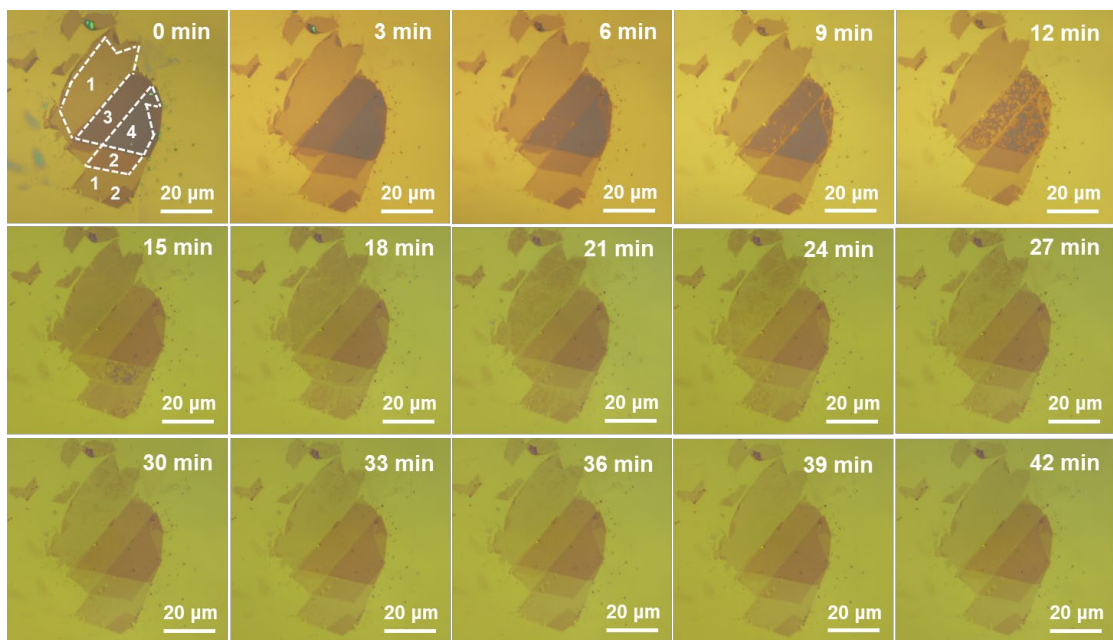


Figure S4. Optical images of the ultrathin step-shaped MoS₂ sample at various stages of the nitridation atomic substitution reaction.

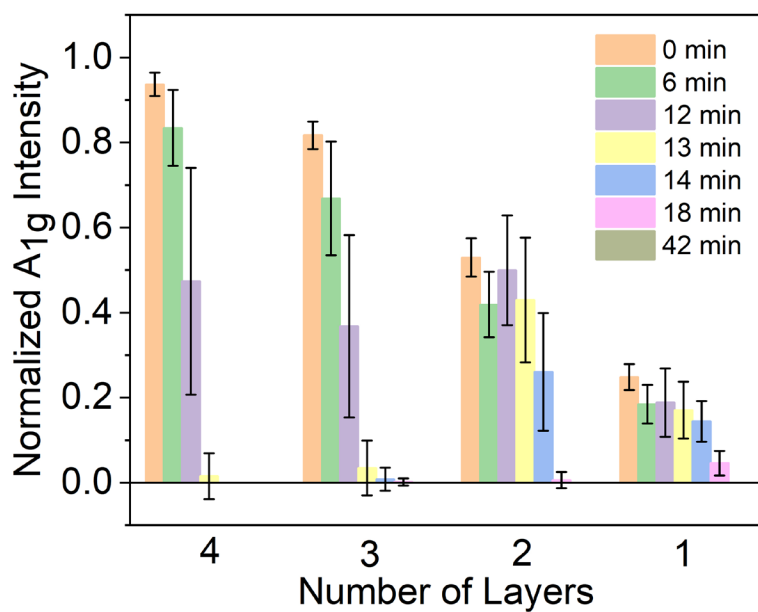


Figure S5. Histogram of the normalized integrated A_{1g} intensity of each thickness region of the ultrathin step-shaped MoS₂ sample at various stages of the reaction.

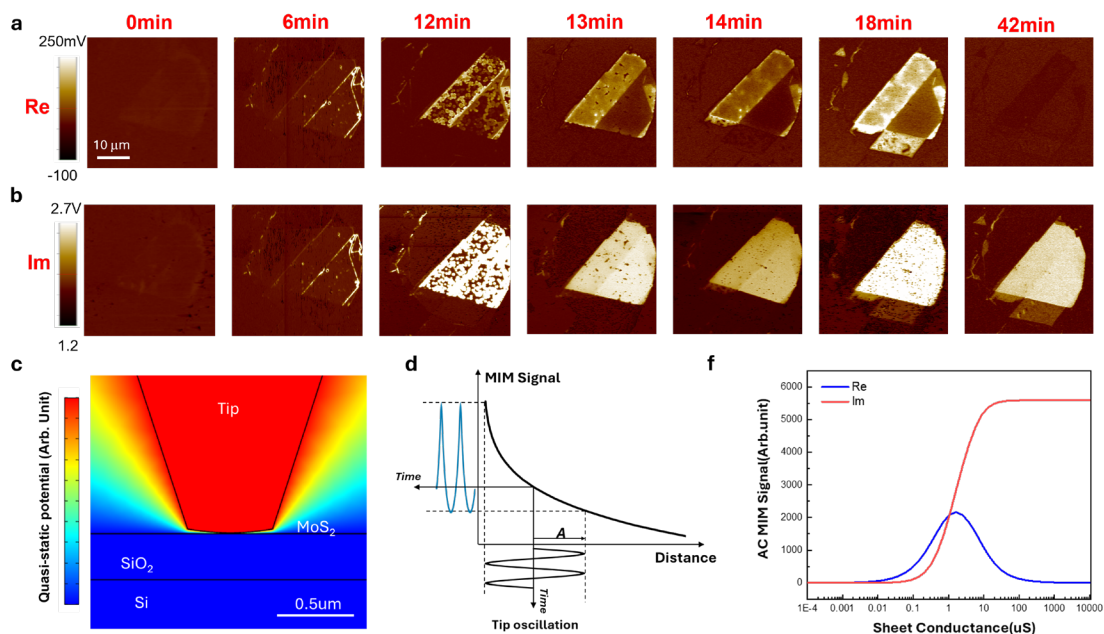


Figure S6. MIM characterization and analysis of the MoS₂ to MoN conversion process with different number of layers. (a) MIM-Re and (b) MIM-Im images of the sample at different stages of the conversion process. (c) Geometry and quasi-static potential distribution in the COMSOL simulation. (d) Simulated DC MIM signal as a function of tip-sample distance, from which the demodulated AC signals can be extracted. (d) Simulated AC MIM signals as a function of 2D sheet conductance.

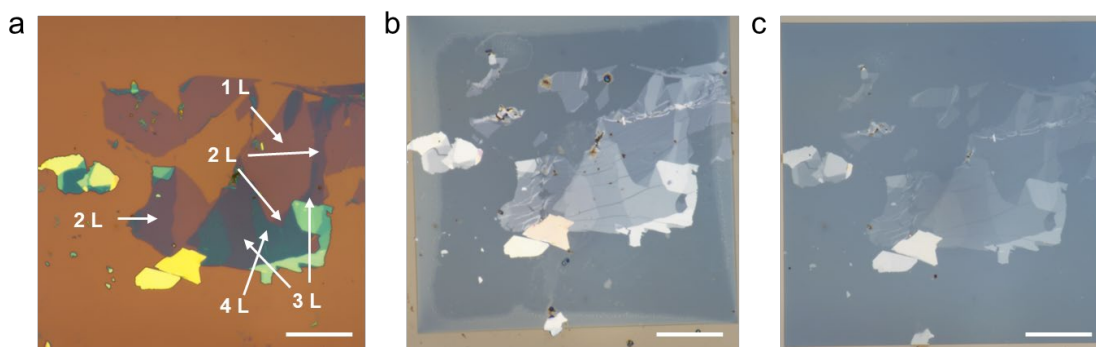


Figure S7. Optical images of the MoS₂ sample for TEM characterization. (a) On a SiO₂/Si substrate; (b) After being transferred to a TEM grid; (c) After nitridation reaction for 90 mins. Scale bars are 10 μm.

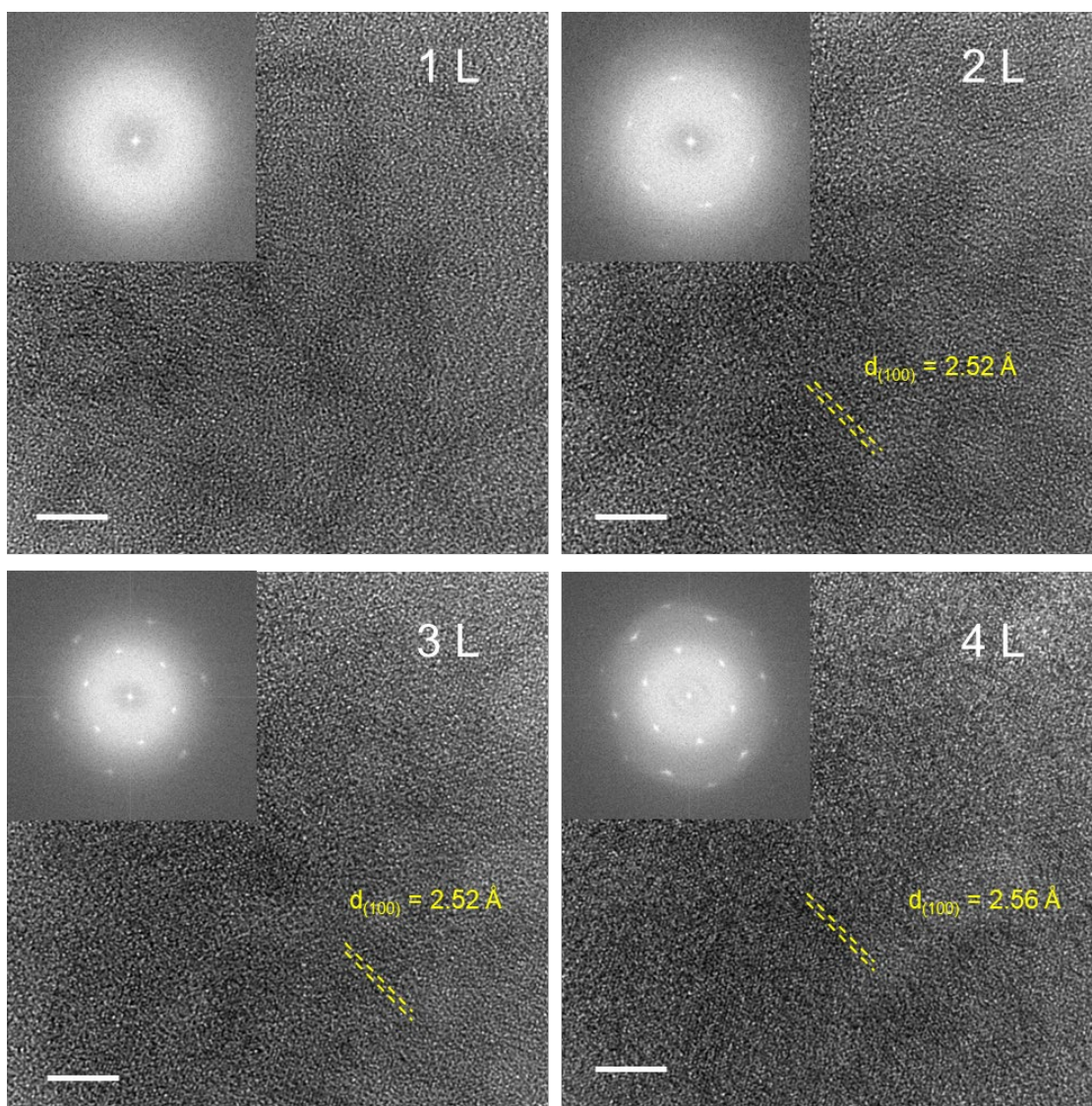


Figure S8. HR-TEM images of MoN crystals converted from 1L, 2L, 3L, and 4L MoS₂, with the d-spacing of δ -MoN (100) planes labeled. Insets are corresponding fast Fourier transform (FFT) patterns. Scales bars are 5 nm.

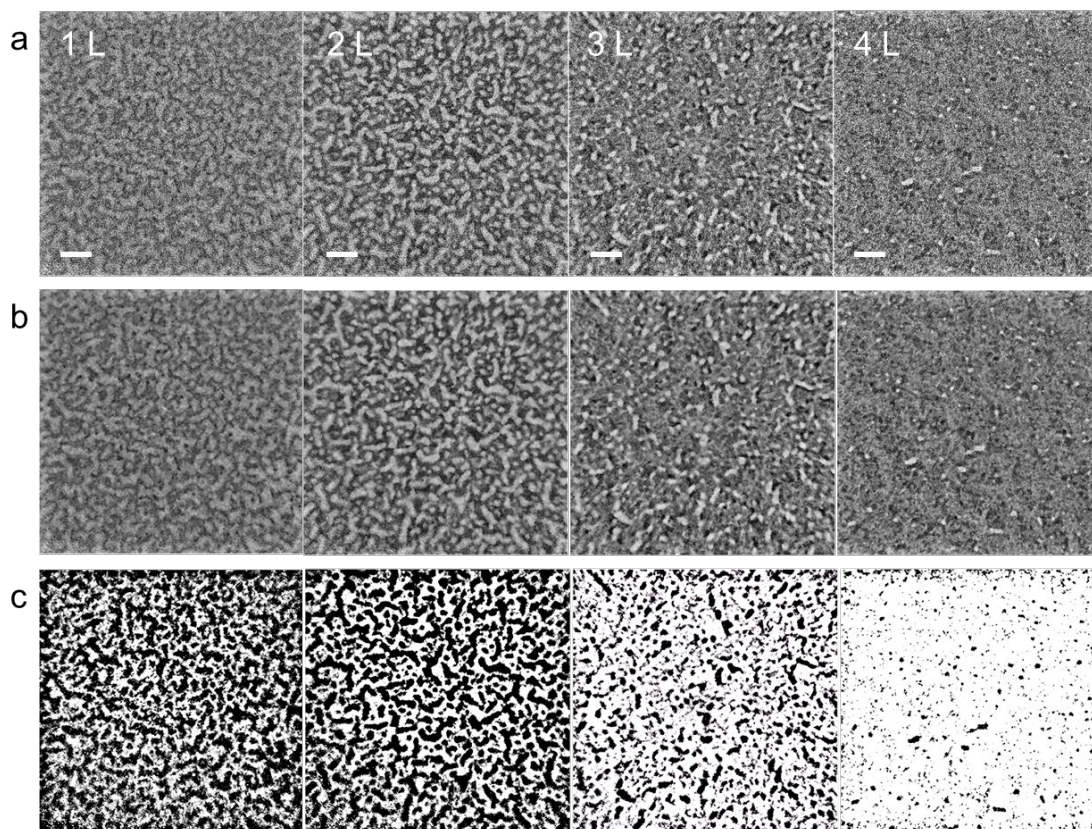


Figure S9. HR-TEM images of MoN structures converted from 1L, 2L, 3L, and 4L MoS₂. (a) Original TEM images; (b) Image after CLAHE-based contrast and illumination correction; (c) Final processed image used for coverage calculation. Scales bars are 20 nm.

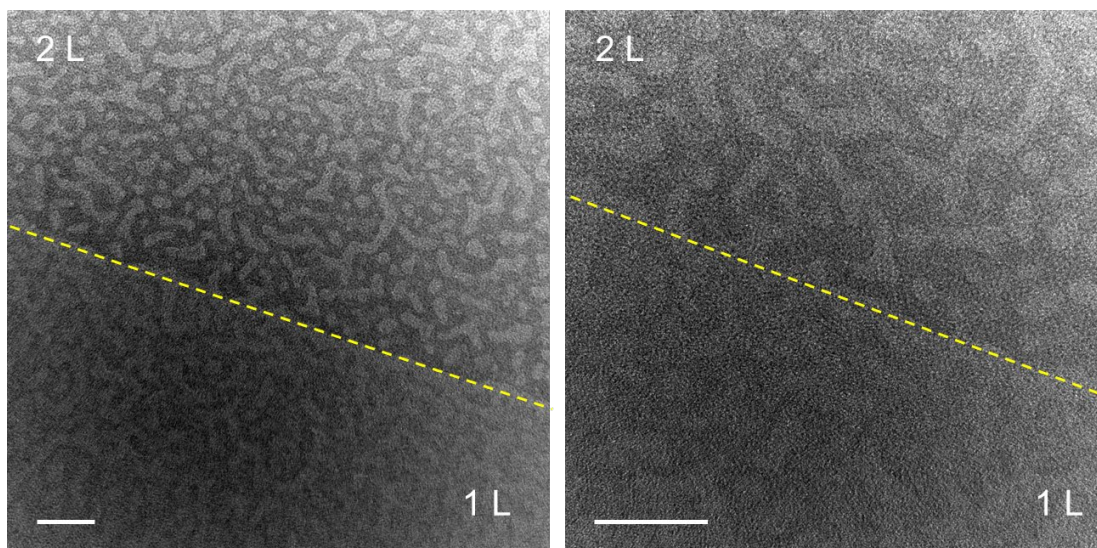


Figure S10. TEM images measured at the boundaries between MoN structures converted

from 1L and 2L MoS₂. Scale bars are 20 nm.

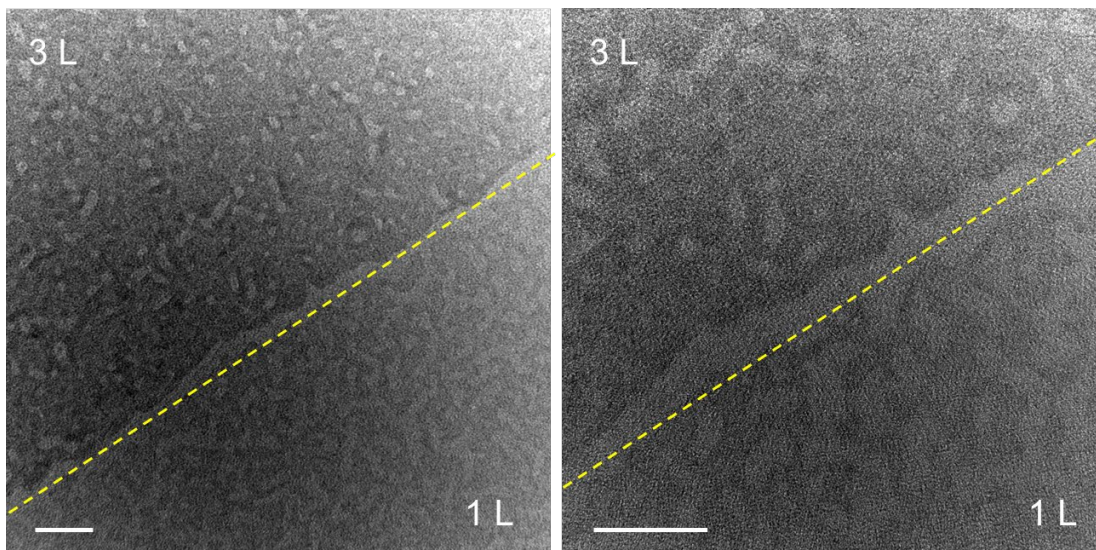


Figure S11. TEM images measured at the boundaries between MoN structures converted from 1L and 3L MoS₂. Scale bars are 20 nm.

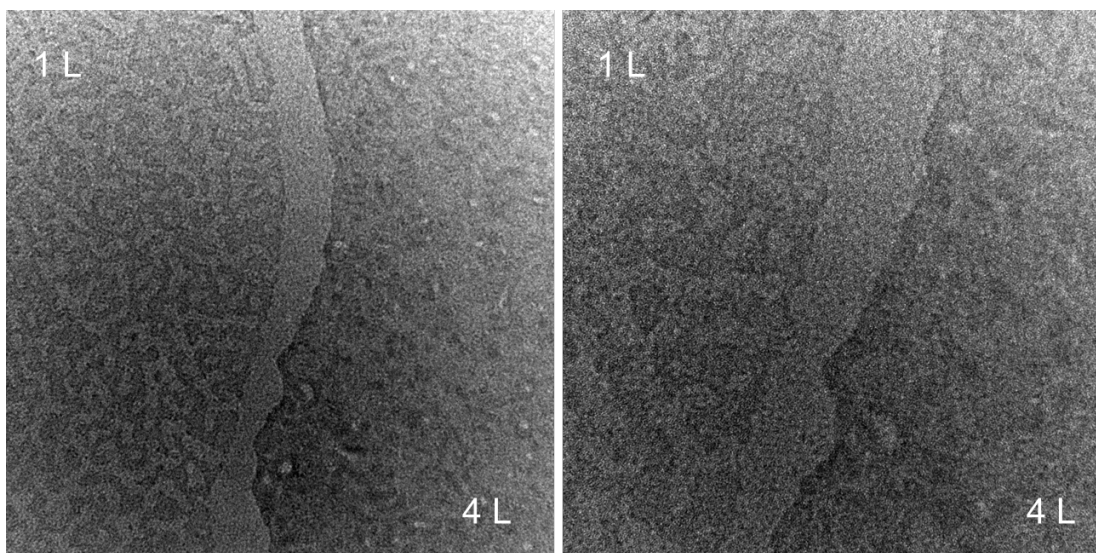


Figure S12. TEM images measured at the boundaries between MoN structures converted from 1L and 4L MoS₂. Scale bars are 20 nm.

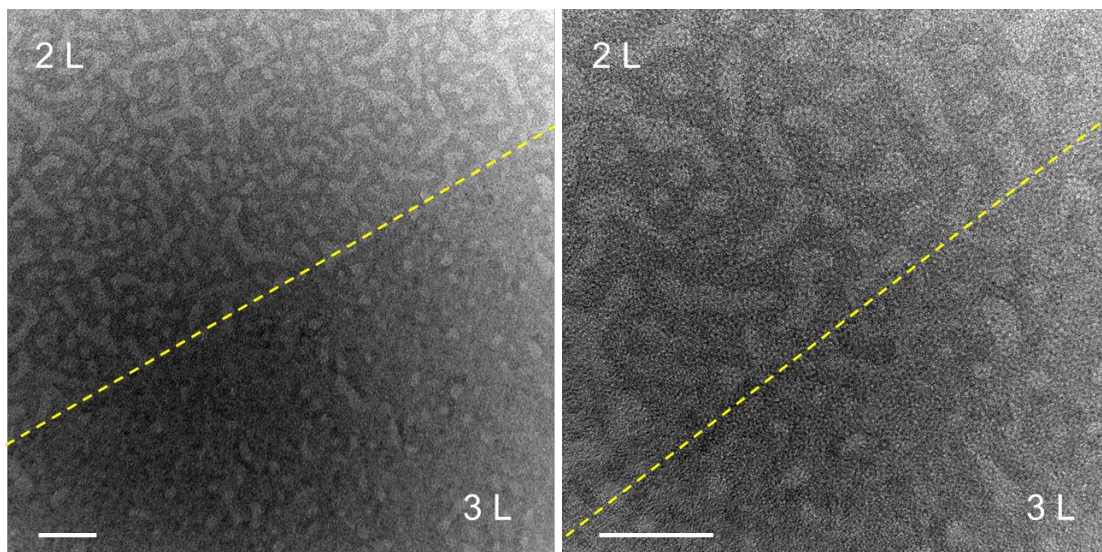


Figure S13. TEM images measured at the boundaries between MoN structures converted from 2L and 3L MoS₂. Scale bars are 20 nm.

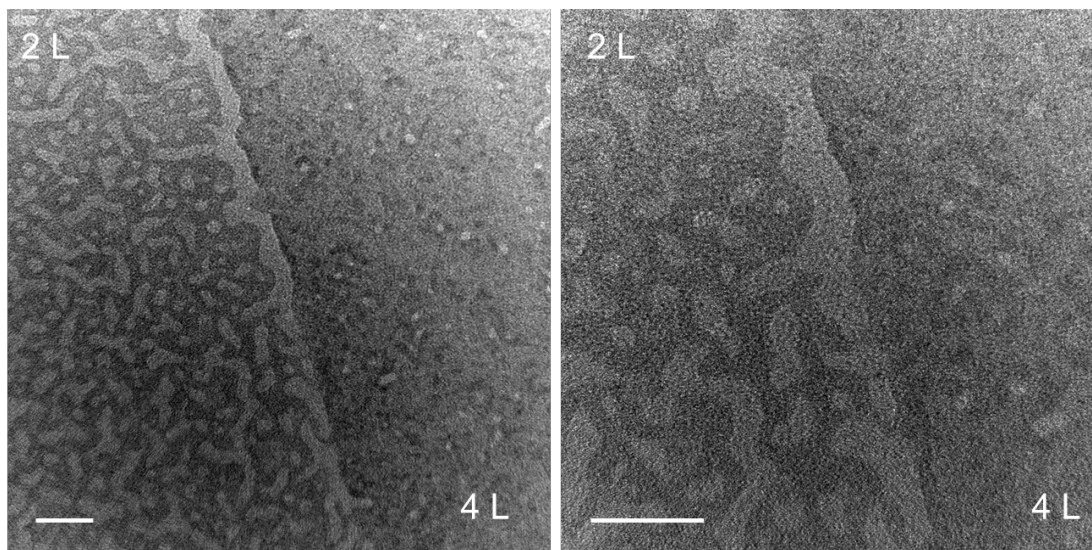


Figure S14. TEM images measured at the boundaries between MoN structures converted from 2L and 4L MoS₂. Scale bars are 20 nm.

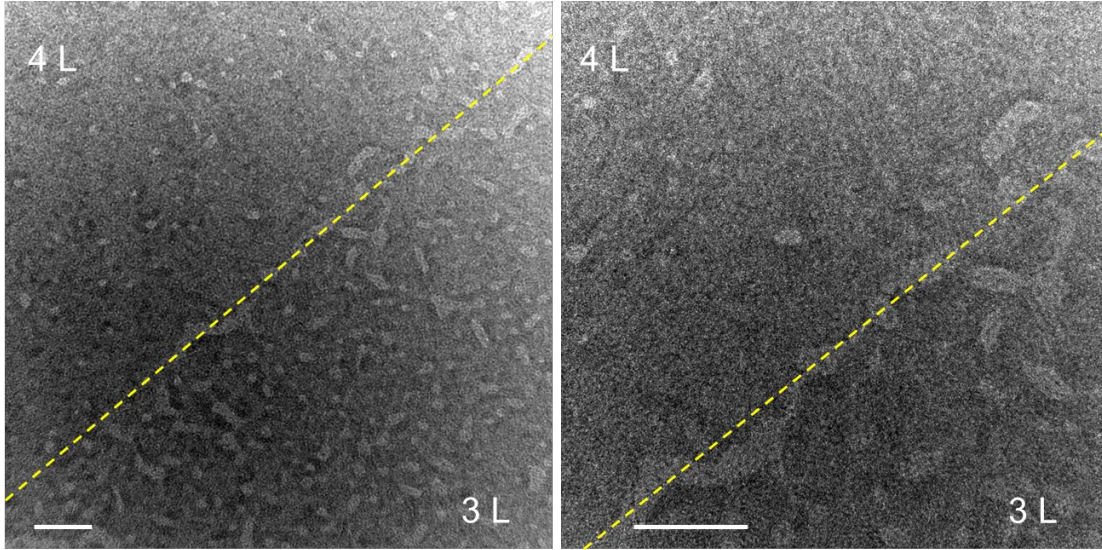


Figure S15. TEM images measured at the boundaries between MoN structures converted from 3L and 4L MoS₂. Scale bars are 20 nm.

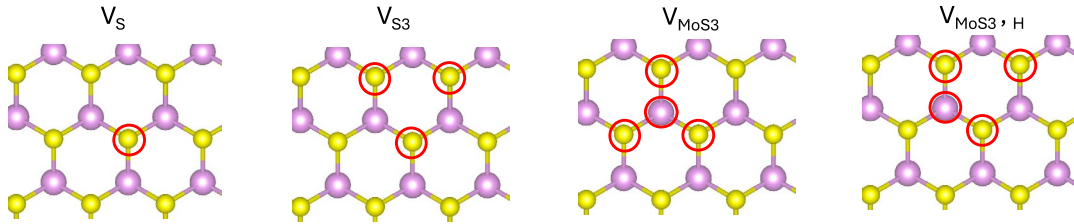


Figure S16. Schematics showing the vacancy position for each defect structure. The red circles indicate that atom was removed from the MoS₂ surface to create a vacancy.

Figure S15 shows the four defect complexes studied with DFT. Table S1 reports the formation energies for each of these defects calculated as,

$$E_{form} = E_{MoS_2+V} - E_{MoS_2} + (N_S \times E_S) + (N_{Mo} \times E_{Mo})$$

where E_{MoS_2+V} is the energy of the MoS₂ surface with the vacancy, E_{MoS_2} is the energy of the pristine MoS₂ surface, E_S (E_{Mo}) is the energy of a single S (Mo) atom, N_S (N_{Mo}) is the number of sulfur (molybdenum) atoms removed. As seen in the table, V_S has the lowest formation energy, and is therefore the most likely defect, followed by V_{S3} and the two V_{MoS3} defects. This finding is consistent with previous studies on MoS₂ defects.¹² We note that for the formation energies, a $3 \times 3 \times n$ supercell is sufficiently converged for

the single sulfur vacancy, so it is used in place of the larger $6 \times 6 \times n$ supercell used for all binding energy calculations in the work.

Table S1. Calculated formation energies for the four vacancy-type point defects considered in this study.

<i>Defect</i>	Supercell	E_{form} (eV)
V_S	331	2.6
V_{S3}	661	8.08
V_{MoS3}	881	9.6
V_{MoS3}, H	881	11.43

References

- (1) Shan, J.-Y.; Morrison, N.; Chen, S.-D.; Wang, F.; Ma, E. Y. Johnson-Noise-Limited Cancellation-Free Microwave Impedance Microscopy with Monolithic Silicon Cantilever Probes. *Nat Commun* **2024**, *15* (1), 5043. <https://doi.org/10.1038/s41467-024-49405-8>.
- (2) Pizer, S. M.; Amburn, E. P.; Austin, J. D.; Cromartie, R.; Geselowitz, A.; Greer, T.; ter Haar Romeny, B.; Zimmerman, J. B.; Zuiderveld, K. Adaptive Histogram Equalization and Its Variations. *Comput Vis Graph Image Process* **1987**, *39* (3), 355–368. [https://doi.org/10.1016/S0734-189X\(87\)80186-X](https://doi.org/10.1016/S0734-189X(87)80186-X).
- (3) Kresse, G.; Furthmüller, J. Efficient Iterative Schemes for Ab Initio Total-Energy Calculations Using a Plane-Wave Basis Set. *Phys Rev B* **1996**, *54* (16), 11169–11186. <https://doi.org/10.1103/PhysRevB.54.11169>.
- (4) Kresse, G.; Furthmüller, J. Efficiency of Ab-Initio Total Energy Calculations for Metals and Semiconductors Using a Plane-Wave Basis Set. *Comput Mater Sci* **1996**, *6* (1), 15–50. [https://doi.org/10.1016/0927-0256\(96\)00008-0](https://doi.org/10.1016/0927-0256(96)00008-0).
- (5) Kresse, G.; Hafner, J. Ab Initio Molecular Dynamics for Liquid Metals. *Phys Rev B* **1993**, *47* (1), 558–561. <https://doi.org/10.1103/PhysRevB.47.558>.
- (6) Kresse, G.; Hafner, J. Ab Initio Molecular-Dynamics Simulation of the Liquid-Metal–Amorphous-Semiconductor Transition in Germanium. *Phys Rev B* **1994**, *49* (20), 14251–14269. <https://doi.org/10.1103/PhysRevB.49.14251>.
- (7) Kresse, G.; Hafner, J. Norm-Conserving and Ultrasoft Pseudopotentials for First-Row and Transition Elements. *Journal of Physics: Condensed Matter* **1994**, *6* (40), 8245–8257. <https://doi.org/10.1088/0953-8984/6/40/015>.
- (8) Perdew, J. P.; Burke, K.; Ernzerhof, M. Generalized Gradient Approximation Made Simple. *Phys Rev Lett* **1996**, *77* (18), 3865–3868. <https://doi.org/10.1103/PhysRevLett.77.3865>.
- (9) Blöchl, P. E. Projector Augmented-Wave Method. *Phys Rev B* **1994**, *50* (24), 17953–

17979. <https://doi.org/10.1103/PhysRevB.50.17953>.

- (10) Kresse, G.; Joubert, D. From Ultrasoft Pseudopotentials to the Projector Augmented-Wave Method. *Phys Rev B* **1999**, *59* (3), 1758–1775. <https://doi.org/10.1103/PhysRevB.59.1758>.
- (11) Pulay, P. Convergence Acceleration of Iterative Sequences. the Case of Scf Iteration. *Chem Phys Lett* **1980**, *73* (2), 393–398. [https://doi.org/10.1016/0009-2614\(80\)80396-4](https://doi.org/10.1016/0009-2614(80)80396-4).
- (12) Hong, J.; Hu, Z.; Probert, M.; Li, K.; Lv, D.; Yang, X.; Gu, L.; Mao, N.; Feng, Q.; Xie, L.; Zhang, J.; Wu, D.; Zhang, Z.; Jin, C.; Ji, W.; Zhang, X.; Yuan, J.; Zhang, Z. Exploring Atomic Defects in Molybdenum Disulphide Monolayers. *Nat Commun* **2015**, *6* (1), 6293. <https://doi.org/10.1038/ncomms7293>.